Influence of Microstructure on High-Cycle Fatigue of Ti-6Al-4V: Bimodal vs. Lamellar Structures

R.K. NALLA, B.L. BOYCE, J.P. CAMPBELL, J.O. PETERS, and R.O. RITCHIE

The high-cycle fatigue (HCF) of titanium alloy turbine engine components remains a principal cause of failures in military aircraft engines. A recent initiative sponsored by the United States Air Force has focused on the major drivers for such failures in Ti-6Al-4V, a commonly used turbine blade alloy, specifically for fan and compressor blades. However, as most of this research has been directed toward a single processing/heat-treated condition, the bimodal (solution-treated and overaged (STOA)) microstructure, there have been few studies to examine the role of microstructure. Accordingly, the present work examines how the overall resistance to high-cycle fatigue in Ti-6Al-4V compares between the bimodal microstructure and a coarser lamellar (β-annealed) microstructure. Several aspects of the HCF problem are examined. These include the question of fatigue thresholds for through-thickness large and short cracks; microstructurally small, semi-elliptical surface cracks; and cracks subjected to pure tensile (mode I) and mixed-mode (mode I + II) loading over a range of load ratios (ratio of minimum to maximum load) from 0.1 to 0.98, together with the role of prior damage due to sub-ballistic impacts (foreign-object damage (FOD)). Although differences are not large, it appears that the coarse lamellar microstructure has improved smooth-bar stress-life (S-N) properties in the HCF regime and superior resistance to fatigue-crack propagation (in pure mode I loading) in the presence of cracks that are large compared to the scale of the microstructure; however, this increased resistance to crack growth compared to the bimodal structure is eliminated at extremely high load ratios. Similarly, under mixed-mode loading, the lamellar microstructure is generally superior. In contrast, in the presence of microstructurally small cracks, there is little difference in the HCF properties of the two microstructures. Similarly, resistance to HCF failure following FOD is comparable in the two microstructures, although a higher proportion of FOD-induced microcracks are formed in the lamellar structure following high-velocity impact damage.

I. INTRODUCTION

A1992 study conducted by the Scientific Advisory Board of the United States Air Force targeted high-cycle fatigue (HCF) as the single largest cause of turbine engine failures in military aircraft.[1] HCF can result in essentially unpredictable failures of engine components, particularly turbine blades, due to the premature initiation of fatigue cracks at small defects and their rapid propagation under high-frequency vibratory loading. To address this problem, a consortium of industrial, government, and academic programs was charged with the overall task of modifying existing design methodologies for improved HCF reliability. These programs have largely focused on a single alloy, Ti-6Al-4V, in a single microstructural condition, namely, the solution-treated and overaged (STOA) or bimodal condition, which is typically used for blade and disk applications in the front (low-temperature) stages of the engine. The current study seeks to extend these observations for the standard bimodal Ti-6Al-4V microstructure to a fully lamellar β-annealed microstructure in the same alloy and to specifically compare the relative merits of these two microstructures for HCF applications.

II. BACKGROUND

The problem of HCF in turbine components is typically associated with a variety of drivers,[2] which vary with the location of interest (Figure 1). In general, components such as blades and disks are subjected to HCF loading associated with the high-frequency (>1 kHz) vibrations in the engine, superimposed onto a low-cycle fatigue component associated with the start-to-stop cycles.[2,3] In the case of blades, this leads to a large variation in load ratios (the ratio (R) of minimum to maximum loads) throughout the component; in particular, the superposition of centrifugal loading on the HCF vibrations can lead to very high R-values which approach unity. On the airfoil section of the blade, HCF cracks can initiate at sites of foreign-object damage (FOD) caused by the ingestion of debris into the engine;[4] here, the problem involves impact-induced residual stresses, microstructural distortion, incipient microcrack formation,

R.K. NALLA, Graduate Student, and R.O. RITCHIE, Professor, are with the Department of Materials Science and Engineering, University of California, Berkeley, CA 94720-1760. B.L. BOYCE, formerly Graduate Student with the Department of Materials Science and Engineering, University of California, is Senior Member, Technical Staff, Sandia National Laboratories, Albuquerque, NM 87185-1411. J.P. CAMPBELL, formerly Graduate Student with the Department of Materials Science and Engineering, University of California, is Senior Manufacturing Engineer, Metals Fabrication Division, General Motors, Troy, MI 48084. J.O. PETERS, formerly Post-doctoral Researcher with the Department of Materials Science and Engineering, University of California, is Research Associate, Technische Universität Hamburg-Harburg, D-21073 Hamburg, Germany.

This article is based on a presentation made in the symposium entitled "Defect Properties and Mechanical Behavior of HCP Metals and Alloys" at the TMS Annual Meeting, February 11–15, 2001, in New Orleans, Louisiana, under the auspices of the following ASM committees: Materials Science Critical Technology Sector, Structural Materials Division, Electronic, Magnetic & Photonic Materials Division, Chemistry & Physics of Materials Committee, Joint Nuclear Materials Committee, and Titanium Committee.

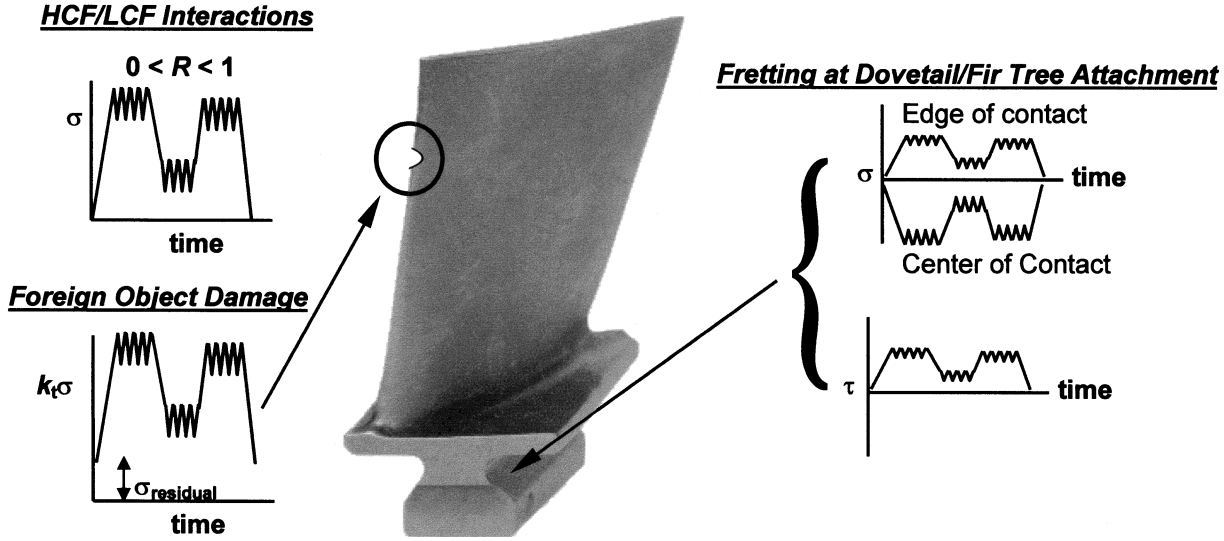

Fig. 1—Diagram illustrating the variety and range of factors involved in HCF failure.

and a geometric stress concentration. Another critical site for crack initiation is in the attachment section of the blade, where contact between the blade dovetail and disk can lead to the formation of fretting fatigue cracks;[5] this problem involves complex multiaxial loading conditions, surface damage, and associated residual stresses.

Current design methodologies for HCF utilize traditional stress-life (S-N) and Goodman diagram approaches, often applied with large safety factors to account for uncertainties in the understanding of the problem. However, because of the extremely high frequencies involved (*i.e.*, parts can experience 10^6 cycles in much less than 1 hour), once a crack starts propagating, failure can ensue rapidly, sometimes within a single flight. Consequently, alternative fracture-mechanics design methodologies, based on the concept of a threshold stress intensity for no crack growth, may offer a preferred approach, provided such thresholds are defined under representative HCF conditions involving small defects subjected to high-frequency, high-load-ratio loading.

Because of the wide range of drivers associated with HCF, selection of a HCF-resistant microstructure in Ti-6Al-4V is not a straightforward task. Indeed, a microstructure that is superior in one region or under one set of HCF conditions may well be deleterious in another region or set of conditions. For example, coarse lamellar microstructures in some titanium alloys often show superior toughness and fatigue-crack growth behavior in the presence of large cracks compared to finer equiaxed microstructures, yet at the same time display inferior fatigue endurance strengths and small-crack behavior (*e.g.*, Reference 6). There is indeed extensive literature on the role of microstructure in influencing the fatigue-crack growth of $\alpha + \beta$ titanium alloys (*e.g.*, References 7 through 17). For example, recent reviews by Lütjering[7] and Thompson[8] summarized the effects of scale and arrangement of α and β phases on the fatigue properties of $\alpha + \beta$ titanium alloys.

Basically, coarse grained, so-called lamellar microstructures with large β grains (~1 mm) and a lamellar matrix of alternating α and β plates can be produced by heat treatment in the high-temperature β-phase field and subsequent slow cooling into the $\alpha + \beta$–phase field. The characteristic microstructural feature of slow-cooled lamellar microstructures is the α colony (~200 to 400 μm), a packet of aligned α plates with the same crystallographic orientation. Finer-scaled microstructures can be processed by faster cooling rates from the β-phase field, resulting in a martensitic type of microstructure with individual oriented α plates (plate width ~1 μm), or by deformation and recrystallization procedures in the $\alpha + \beta$–phase field, where the recrystallization temperature determines the volume fraction and size of equiaxed primary α phase. So-called bimodal microstructures consist of a low volume fraction of primary α grains (~15 to 30 pct, ~20 μm) with a colony-type lamellar matrix of alternating α and β plates within small β grains (20 to 40 μm).

The most critical parameter to increase the HCF strength (resistance against fatigue-crack nucleation) is to reduce the maximum dislocation slip length in the microstructure.[9] Generally, fatigue cracks nucleate due to irreversible slip within the longest crystallographic slip bands (*i.e.*, maximum slip length) available in the microstructure. Consequently, coarse lamellar microstructures with colonies of aligned α and extended planar slip across these colonies often have a lower HCF strength as compared to fine-grained equiaxed and martensitic α-plate-type microstructures with concomitant reduced effective slip lengths.[10,11]

The preference for propagation of naturally initiated small surface cracks along specific crystallographic planes combined with an aligned orientation of α plates into colonies allows the crack to cross an entire colony as if it were a single microstructural unit. This propagation mechanism along planar slip bands is very fast in coarse lamellar microstructures because of the much larger slip length as compared to finer-scaled microstructures. Fine-grained and martensitic microstructures tend to slow the propagation rates of small cracks due to the higher density of grain boundaries or individual α plates acting as obstacle points.[12,13,14]

However, this ranking between coarse lamellar and fine-grained microstructures is reversed with increasing crack length.[12,14–16] Lamellar microstructures in $\alpha + \beta$ titanium

Table I. Chemical Composition of Ti-6Al-4V Bar Stock (in Weight Percent)[28]

Bar Location	Ti	Al	V	Fe	O	N	H
Top	bal	6.27	4.19	0.20	0.18	0.012	0.0041
Bottom	bal	6.32	4.15	0.18	0.19	0.014	0.0041

alloys exhibit superior fatigue-crack growth resistance compared to fine-grained microstructures when these properties are measured using large cracks, which are on the order of several millimeters (or at least many times the microstructural unit size). It is found that crack growth into adjoining, but differently oriented, α colonies involves pronounced crack deflection, crack bifurcation, and secondary crack formation, because of the limited number of slip systems available within the hcp α phase. Therefore, the superior crack-growth resistance in a colony-type lamellar microstructure is attributed to a crack path characterized by a high degree of crack deflection, bifurcation, and secondary cracking and, at low load ratios, also by a high degree of (roughness-induced) crack closure.[12,16–18] Indeed, Yoder *et al.*[17] pointed out that lamellar microstructures with reduced colony sizes had less resistance against crack propagation. Also, crack growth in fine equiaxed microstructures did not cause large crack deflections because of the smaller-sized microstructural features.[12,14]

It should be noted that most of these data, specifically for Ti-6Al-4V, pertain to lower frequencies and large (>5 mm), through-thickness cracks (*e.g.*, References 18 through 26), which are not necessarily appropriate for the present HCF scenario, where frequencies are in excess of 1 to 2 kHz and the relevant crack sizes are on the order of fractions of a millimeter and can grow at stress intensities well below the established large-crack fatigue thresholds for the material.[27] Consequently, to evaluate the general susceptibility of Ti-6Al-4V alloys to HCF, in the present article, the HCF properties of the bimodal and lamellar microstructures are compared. In view of the complexity of the problem, many facets of HCF behavior are examined, including the effect of load ratio, mode-mixity, crack size, and pre-existing impact damage.

III. MATERIALS AND EXPERIMENTAL PROCEDURES

A. *Materials and Microstructures*

The Ti-6Al-4V alloy used in this study originated as double vacuum-arc remelted forging stock produced by Teledyne Titanium (Pittsburgh PA) specifically for the joint government-industry-academia HCF program. The chemical composition of this alloy is given in Table I.[28]

1. *Bimodal microstructure*

The original bar stock (63.5 mm in diameter) was sectioned into segments 400-mm long, preheated to 940 °C for 30 minutes, and forged as glass-lubricant–coated bars at this temperature into 400 × 150 × 20 mm plates.[28] These plates were solution treated at 925 °C for 1 hour, fan air cooled, and then stabilized at 700 °C for 2 hours. The microstructure of the STOA condition consisted of a bimodal distribution of interconnected equiaxed primary α grains and lamellar $\alpha + \beta$ colonies (transformed β) (Figure 2(a)). A careful

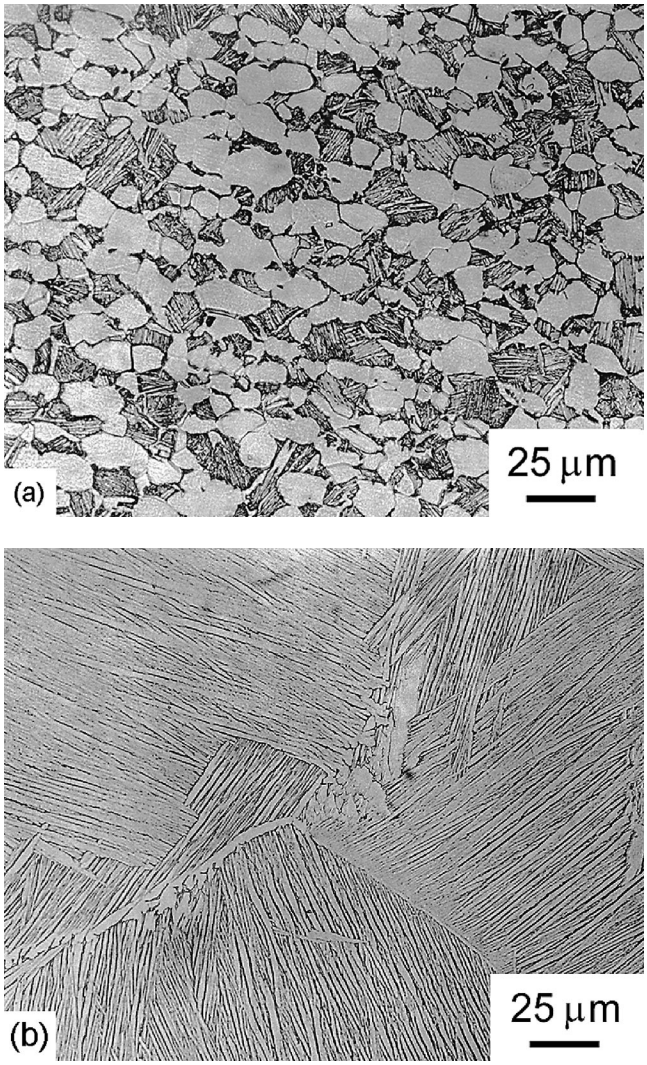

Fig. 2—Optical micrographs of the microstructures of Ti-6Al-4V: (*a*) bimodal (solution treated and overaged, STOA) and (*b*) lamellar (β annealed). Etched for ~10 s in 5 parts 70 pct HNO_3, 10 parts 50 pct HF, and 85 parts of H_2O.

investigation of the relative distribution of phases indicated an overall primary α content of 64 pct. The average grain size obtained was ~20 μm, with a slight grain elongation observed in the longitudinal (L) direction of the forging. Using differential thermal analysis, the β-transus temperature was measured to be 990 °C to 1005 °C.

2. *Lamellar microstructure*

To compare with the bimodal Ti-6Al-4V structure, a fully lamellar microstructure was also examined. This microstructure (Figure 2(b)) was obtained by solution treating in a vacuum of 10^{-5} to 10^{-6} mbar at 1005 °C (slightly above the β-transus temperature) for 10 to 30 minutes (depending on the cross section), followed by a rapid quench (~100 °C/min)* in high-purity helium gas. The microstructure thus obtained was stabilized at 700 °C for 2 hours *in vacuo*, before slow furnace cooling to room temperature. The resulting Widmanstätten microstructure had an average prior-β grain

*This quench rate was chosen to achieve a similar lath spacing of the transformed β in the two microstructures.

Table II. Uniaxial Tensile and Toughness Properties of Ti-6Al-4V

Microstructure	Yield Strength (MPa)	Ultimate Tensile Strength (MPa)	Reduction in Area (Pct)	Fracture Toughness K_{Ic} (MPa $\sqrt{m}$)
Bimodal	930	978	45	64
Lamellar	975	1055	10	100

size of ~1 mm, a colony size (parallel-oriented α-phase lamellae) of 500 μm, and an average α lamellae lath width of 1 to 2 μm, similar to the interlamellar spacing of the transformed β in the bimodal microstructure.

B. *Mechanical Testing*

1. *Uniaxial tensile and toughness properties*

Uniaxial tensile tests were conducted in both microstructures in the L-orientation using strain rates of 5×10^{-4} s^{-1}; additional data for the bimodal microstructure were taken from Reference 28. Results in terms of the strength, ductility, and toughness are given in Table II. The lamellar structure exhibited somewhat higher strength levels, whereas the bimodal structure exhibited over a factor-of-4 higher ductility, due to its smaller grain size, which limited the effective slip length. Despite its lower ductility, plane-strain fracture toughness values, measured using 25-mm-thick, precracked compact-tension specimens, were over 50 pct higher in the lamellar microstructure; similar observations have been made in previous studies (*e.g.*, Reference 29).

2. *Smooth-bar stress-life (S-N) fatigue testing*

To evaluate the smooth-bar stress-life (S-N) fatigue properties of both microstructures, fatigue tests were performed in room-temperature air (25 °C, 35 to 45 pct relative humidity) under load control at positive load ratios of $R = 0.1$ and 0.5, on servohydraulic testing machines cycling at 25 Hz (for lives $<10^6$ cycles) and at 1000 Hz (for lives $> 10^6$ cycles) on unnotched hourglass specimens with threaded grip sections and minimum gage diameters of 3.0 mm (25 Hz) and 5.4 mm (1000 Hz).* The specimen axis was aligned parallel to the length of the plate (L-orientation). For the bimodal microstructure, results were supplemented with 85 Hz S-N data from Reference 14 on the same material.

To achieve a nominally stress-free surface prior to fatigue testing, samples in both microstructures were stress relieved *in vacuo* for 2 hours at 705 °C prior to chemically milling in a solution of 50 mL HF, 500 mL HNO_3 and 1500 mL H_2O. Similar procedures were used for the small-crack and FOD test samples.

3. *Fatigue-crack growth testing in pure mode I*

Large-crack tests: Mode I fatigue-crack propagation studies, on through-thickness cracks which were large compared to the scale of the microstructure (>4 mm), were carried out for both microstructures using 8-mm-thick compact-tension specimens (of 25.4-mm width) machined in the L-T orientation. To facilitate observation of crack propagation, after machining the specimen sides were ground to a 1200-grit finish before chemically polishing to a finish of 0.05 μm. Samples were first fatigue precracked for a minimum of ~2 mm from the notch tip using initial ΔK levels of 8 to 15 MPa$\sqrt{m}$. This was carried out at the same load-shedding rate and load ratio as was subsequently used for the actual test, as described subsequently.

Fatigue-crack growth testing was performed in accordance with ASTM Standard E 647 in room-temperature air under load control, with crack lengths monitored *in situ* using back-face strain (BFS) compliance techniques. Two techniques were used to determine the alternating and maximum stress intensities at the threshold, (ΔK_{TH} and $K_{max,TH}$, respectively), which were defined at a propagation rate of 10^{-10} to 10^{-11} m/cycle. Standard constant-R testing for load ratios between 0.1 and 0.8 was performed by load shedding toward the threshold using the scheme $\Delta K = \Delta K_{initial} \exp(C(a - a_{initial}))$, with the K-gradient (C) set at -0.08 mm^{-1} (ΔK and a are the stress-intensity range and crack length, respectively). In addition, constant-K_{max}/increasing-K_{min} testing* was performed to achieve load ratios approaching unity, using K_{max} values from 26 to 57 MPa$\sqrt{m}$ for the bimodal microstructure and 27 to 87 MPa$\sqrt{m}$ for the lamellar microstructure. These procedures, which act to minimize the effect of crack closure, gave thresholds at very high load ratios between 0.89 and 0.98.

A range of frequencies between 50 and 1000 Hz was examined; additional ultrasonic fatigue tests at 20,000 Hz[34] were performed on the bimodal microstructure only. Tests at 50 Hz were performed on a standard MTS servohydraulic testing machine; corresponding tests at 200 to 1000 Hz were performed on a newly developed MTS servohydraulic test frame incorporating a voice-coil servovalve. Thresholds were determined using the same procedure described for the constant-R tests. Data are presented in terms of the crack growth rate per cycle (da/dN) as a function of the stress-intensity range ($\Delta K = K_{max} - K_{min}$).*

The magnitude of crack closure was monitored using BFS compliance; specifically, the global closure stress intensity (K_{cl}) was approximated from the point of first deviation from linearity in the elastic compliance curve on unloading.[35] Based on such measurements, an effective (near-tip) stress intensity ($\Delta K_{eff} = K_{max} - K_{cl}$) was estimated.

Small-crack tests: Corresponding mode I fatigue-crack-propagation testing on microstructurally small (~1 to 50 μm) surface cracks was performed by periodic scanning electron microscopy monitoring of so-called K_B tensile samples, where cracking was initiated at sites of impact damage, as described in Section III–B–5. These samples had a rectangular cross section of 3.2 by 7.2 mm, a gage length of 20 mm, and cylindrical buttonhead ends and were cycled at 25 Hz (for lives $<10^6$ cycles) and 1000 Hz (for lives $>10^6$ cycles) at $R = 0.1$ and 0.5.

Approximate local stress intensities for small cracks

*Based on a comparison of results performed at frequencies up to 1000 Hz by Ritchie *et al.*[30] and ultrasonic fatigue-threshold measurements by Meyer and Stanz–Tschegg, no effect of cyclic frequency has been found in this alloy for fatigue tests between 50 and 20,000 Hz, conducted in ambient-air environments.[31]

*The constant-K_{max}/increasing-K_{min} test for threshold measurements was first developed by Döker *et al.*[32] It was subsequently used by Hertzberg and co-workers to provide a simulation of short-crack growth behavior.[33]

*Note that for simplicity, the mode I stress intensity is referred to as ΔK. However, in sections relevant to the mixed-mode behavior, ΔK_I is used to distinguish the mode I stress intensity from the mode II stress intensity (ΔK_{II}).

formed at the base and crater rim of the damaged sites were calculated from the relationship[36]

$$\Delta K = \frac{0.7\ k_t}{\sqrt{1 + 4.5\ (a/\rho)}}\ \Delta\sigma\sqrt{\pi\, a} \qquad (1)$$

where k_t is the elastic-stress-concentration factor, a is the crack depth, and ρ is the indentation radius. The factor of 0.7 is based on the stress-intensity boundary correction and the crack-shape correction factor,[37] the crack shape being determined from fractographic observations as $a/2c \sim 0.45$ (a is the crack depth and $2c$ is the surface-crack length).*

*The exact shape of such small surface cracks and the variation in this aspect ratio with crack extension clearly can have an important effect on the crack driving force and, hence, the crack-growth behavior.[38,39] In the current work, for small-crack threshold determination, the exact aspect ratios were obtained by postfractographic observations. For crack-growth-rate studies, a constant aspect ratio was assumed, although our crack-shape studies, described in Reference 40, did indicate that this was a reasonable assumption.

Despite the physically small size of the cracks, the use of the stress intensity was justified here, as maximum plastic zone sizes were only ~0.2 to 1 μm for 1 to 10-μm sized cracks at $\Delta K \sim 1$ to 2 MPa$\sqrt{\text{m}}$ conditions were, thus, close to that of small-scale yielding. However, it should be noted that Eq. [1] does not take into account the presence of the impact-induced residual stresses, although these stresses will not change the value of the stress-intensity *range*. Moreover, recent X-ray diffraction studies[41] have shown that at the higher applied stresses, such residual stresses at the base and rim of the damage site tend to relax within the first few fatigue cycles.

4. *Fatigue-crack growth testing under mixed-mode loading*

The corresponding fatigue-crack growth testing under mixed-mode conditions was performed using the asymmetric four-point-bend (AFPB) sample (*e.g.*, Reference 42). This specimen can achieve a range of mode-mixities, essentially from pure mode I to mode II, by changing the crack offset from the load line. Specimens, 11.3-mm wide and 4.5-mm thick, were machined in the L-T orientation. For comparison, pure mode I tests were conducted using symmetric four-point bending, with inner and outer spans of 12.7 and 25.4 mm, respectively. For all samples, the surfaces required for crack-length observation were polished to a 0.05 μm finish, whereas the sides to be used to carry the load-bearing pins were ground down to a 600-grit finish.

a. *Large-crack tests*

Mixed-mode thresholds were determined on the basis of crack initiation from a carefully prescribed precrack, as described in detail elsewhere.[43,44,45] Fatigue precracks were grown from 2-mm-deep electro discharge-machined notches in symmetric four-point bending at $R = 0.1$; the final precrack length was 4.50 ± 0.25 mm, achieved at final ΔK_{I} values of 4.8 ± 0.5 and 6.8 ± 0.5 MPa$\sqrt{\text{m}}$, respectively, for the bimodal and lamellar microstructures. Using recently developed solutions[42] for the values of ΔK_{I} and ΔK_{II} for the AFPB geometry, mixed-mode tests for large (>4 mm) through-thickness cracks were performed at load ratios from 0.1 to 0.8 for mode-mixities varying from pure mode I ($\Delta K_{\text{II}}/\Delta K_{\text{I}} = 0$) to nearly pure mode II ($\Delta K_{\text{II}}/\Delta K_{\text{I}} = 7.1$), corresponding to phase angles ($\beta = \tan^{-1}(\Delta K_{\text{II}}/\Delta K_{\text{I}})$) of 0 to 82 deg, respectively. Each test involved cycling the precracked specimen at the desired mode-mixity, if no crack growth was observed using an optical microscope after 2×10^6 to 5×10^6 cycles, either ΔK_{I} or ΔK_{II} was increased by ~0.25 MPa$\sqrt{\text{m}}$ and the same testing procedure was repeated. In this way, a "growth/no growth" condition bounding the threshold was obtained, with growth being defined to be crack extension on the order of the microstructural dimension (~20 μm for a bimodal and ~500 μm for a lamellar microstructure). Estimates of the extent of crack-tip shielding in both modes I and II were made using a compliance-based technique; as described in Reference 44, this technique involved determining the mode I and mode II compliance curves *in situ* using a crack-opening displacement gage.*

*As described in detail in Reference 44, the distinction between the contributions to shielding in modes I and II is achieved by examining separate load-displacement curves using two gages mounted near the crack tip; these gages are used to measure opening and shear displacements. Mode I shielding, in the form of crack closure, is determined from the compliance curve for the opening displacements, whereas mode II shielding, in the form of asperity rubbing and interlock, is determined in an analogous fashion from the compliance curve for shear displacements.

b. *Short-crack tests**

**Short* cracks are defined here as being small in all but one dimension, compared to *small* cracks, which are small in all dimensions. Further details on the distinction between, and relevance of large, short, and small cracks are given in the Appendix.

Corresponding mixed-mode thresholds for through-thickness short (~200 μm) cracks were obtained in an identical fashion, except that the wake of the precrack was carefully machined away to within ~200 μm of the crack tip using a slow-speed diamond saw. The intent of this procedure was to minimize the extent of crack-tip shielding by reducing the degree of surface contact in the crack wake.

c. *Small-crack tests*

Corresponding mixed-mode thresholds tests for microstructurally small (<50 μm), semi-elliptical surface cracks were performed using an inclined crack technique. A small, semielliptical surface precrack (~10 to 50 μm) was first obtained by standard mode I, three-point bend testing at $R = 0.1$ (50 Hz) of wide (16.3 mm), 5-mm-thick rectangular bars machined in the L-T orientation. Prior to testing, samples were stress-relieved for 2 hours at 675 °C *in vacuo*, and surfaces necessary for observation were polished to a 0.05 μm finish. Once a small crack had initiated, a bend bar was carefully machined from the original wide sample, with the small crack inclined at the desired angle to the axis of the bar. This bar was then subjected to symmetric four-point bending, and the threshold for crack initiation from the inclined crack was determined in a similar manner to that described previously for mixed-mode large-crack testing. Linear-elastic solutions for the stress-intensity ranges for small semielliptical surface cracks in mode I and mixed-mode loading were obtained from References 37 and 46. Exact crack shapes ($a/2c$) were determined following threshold determination by fractographic observations.

5. *Foreign-object damage*

The effect of FOD on the fatigue behavior of Ti-6Al-4V was examined using modified K_B tensile specimens.[40,47,48] The FOD was simulated by firing 3.2-mm-diameter

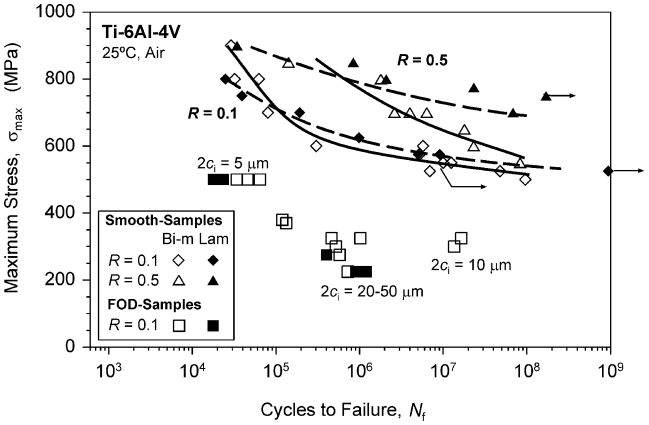

Fig. 3—Smooth-bar stress-life (S-N) data at $R = 0.1$ and 0.5 for the bimodal and lamellar microstructures in Ti-6Al-4V. Data points refer to samples following simulated FOD and clearly show a severely reduced fatigue life due to such damage; numbers adjacent to data points indicate the surface crack length, $2c_i$, of the FOD-induced microcracks.

chrome-hardened steel spheres at velocities between 200 and 300 m/s onto the flat surface of the K_B specimens at an angle of 90 deg, using a compressed-gas gun facility. These velocities represent typical in-service impact velocities on aircraft engine fan blades. The resulting damage craters are also typical of those seen in service, with root radii similar to those of actual damage sites. After impacting, specimens were cycled at 1000 Hz at a stress range ($\Delta\sigma$) between 225 and 500 MPa ($R = 0.1$ and 0.5), and results were compared to the unimpacted smooth-bar S-N data. Throughout the fatigue testing, specimens were periodically removed and examined in a high-resolution field-emission scanning electron microscope in order to monitor crack-initiation and growth in the vicinity of the damage site. Resulting small-crack data are presented in terms of their growth rates as a function of both crack size (a) and the stress-intensity range (ΔK).

Residual stresses surrounding the damage sites were both numerically computed and experimentally measured using synchronous X-ray diffraction.[49] However, relaxation of a significant portion of these stresses was found (from *in-situ* X-ray studies) at the higher applied stresses utilized for these tests.

IV. RESULTS AND DISCUSSION

A. *Smooth-Bar Stress-Life Fatigue*

Smooth-bar S-N curves for the bimodal and lamellar microstructures are shown in Figure 3 for load ratios of 0.1 and 0.5. (The numbers next to individual data points refer to microcrack sizes following FOD, as discussed in Section IV–D). In the high-cycle regime, in this case for lives exceeding $\sim 10^5$ cycles at $R = 0.1$ and 10^6 at $R = 0.5$, the lamellar structure appears to display the superior fatigue properties, with a higher 10^8 cycle endurance strength, particularly at $R = 0.5$. This is consistent with the higher tensile strength of this microstructure. It should be noted, however, that at shorter lifetimes in the low-cycle fatigue regime, it is the bimodal microstructure that appears to show the better fatigue properties, consistent with the higher ductility exhibited by this structure, although in the present study only limited data were collected in this regime. The fact that the lamellar structure appears to show better S/N properties in the HCF regime is somewhat unusual, but may be related to the fact that the bimodal structure studied in this work has a very high percentage (~64 pct) of interconnected primary α, which leads to a large effective slip length; typical bimodal microstructures in Ti-6Al-4V usually consist of only ~30 pct of primary α.

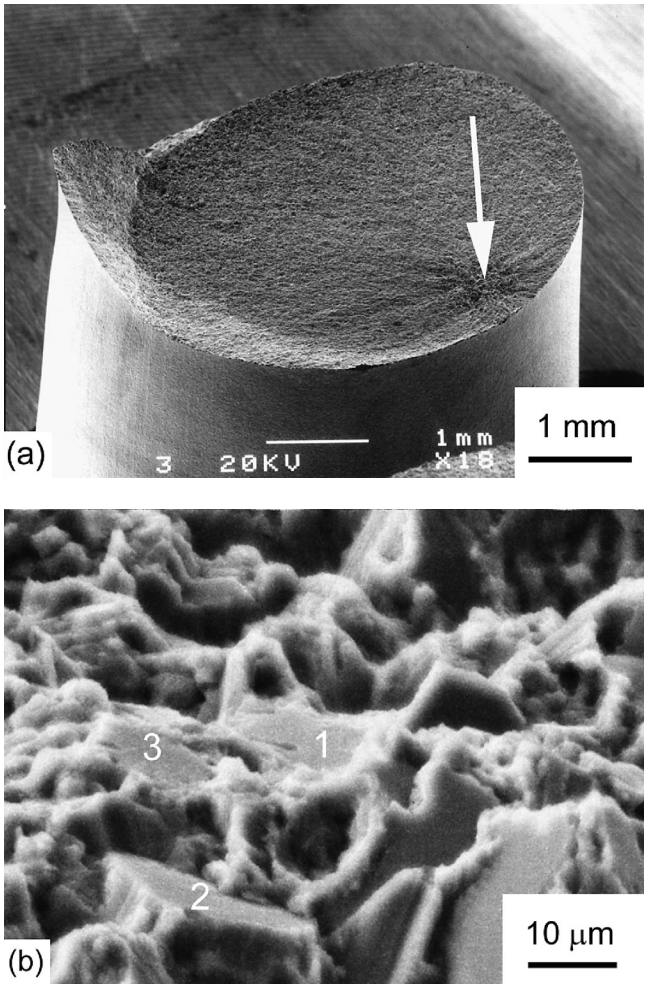

Fig. 4—(*a*) Subsurface fatigue crack, initiation site (arrow) in bimodal Ti-6Al-4V ($R = 0.1$, $\sigma_{max} = 500$ MPa, and $N_f = 9.6 \times 10^7$ cycles), showing (*b*) crack initiation and early growth along planar slip bands leading to facet-type fracture surface (specimen tilt: 70 deg). The EBSD analysis of fractured α grains 1 through 3 revealed near-basal orientation of fracture plane.

Crack initiation, which is generally the dominant stage in smooth-bar HCF, was found to occur both at the surface and subsurface regions of the specimens. Although prior studies[14] in bimodal and lamellar Ti-6Al-4V under tension-compression ($R = -1$) loading showed fatigue cracks to initiate at the surface, for the present work at positive load ratios ($R = 0.1$ and 0.5), crack initiation was often seen in regions close to the surface. For example, crack initiation occurred at ~40 to 100 μm below the surface and extended farther into the interior, some ~250 to 450 μm for the bimodal structure and as deep as ~1 to 2 mm for the lamellar structure.

Typical subsurface initiation sites in the bimodal microstructure were characterized by a faceted fracture surface (Figure 4), caused by the cracking of suitably oriented α

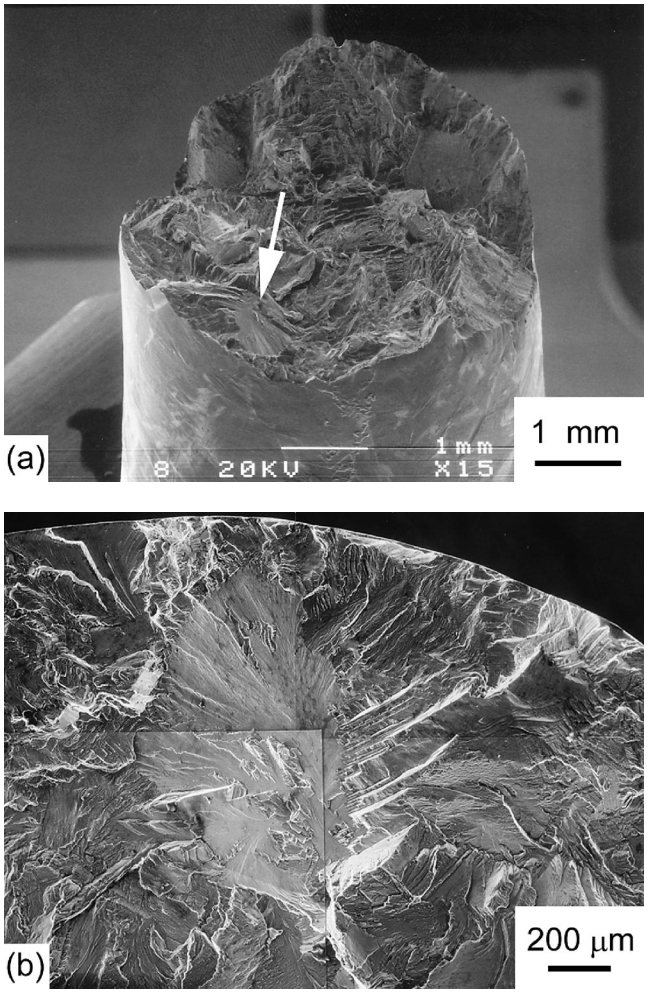

Fig. 5—Subsurface fatigue crack initiation site (arrow) in lamellar Ti-6Al-4V ($R = 0.5$, $\sigma_{max} = 700$ MPa, and $N_f = 6.8 \times 10^7$ cycles), showing (*b*) cross-colony slip band crack initiation and early growth along macroscopically planar facets of colony width dimensions (~500 μm).

grains and subsequent growth along planar slip bands within interconnected α grains (Figure 4(a)). Electron back scattered diffraction (EBSD) analysis revealed that many of these α grains were aligned with a near-basal orientation perpendicular to the stress axis (Figure 4(b)). Subsurface crack-initiation sites in fully lamellar Ti-6Al-4V were characterized by cross-colony slip-band fracture (Figure 5), typically of colony-width dimensions (~500 μm). Such slip bands can form across an entire colony where the laths are of similar orientation and the surrounding β layers are extremely thin.[8] Current studies are focused on crystallographic analysis of cross-colony fracture facets, which are also associated with a near-basal orientation,[50,51] as shown by the cracked α grains of the bimodal microstructure.

Such subsurface crack initiation is not common in fatigue, but has become increasingly reported of late for fatigue failures under very-long-life conditions in steels (*e.g.*, Reference 52); however, it is more frequently encountered in titanium alloys.[51,53–55] Most traditional explanations for this phenomenon rely on the presence of processing-induced, surface compressive residual stresses, *i.e.*, due to heat treatment, case-hardening, or shot-peening procedures. Other explanations include the formation of such compressive residual stresses due to preferential plastic deformation at the surface under tension-tension loading[54] and the higher probability of finding a stress-raising defect (*e.g.*, inclusions in steels) or a weak microstructural orientation or "hard" α particle (in titanium alloys) in the bulk of the material compared to the surface. As nominally stress-free surfaces were employed in the present study, it is believed that the subsurface initiation is the result of the latter effect. In particular, the high fatigue strength of lamellar Ti-6A1-4V may be due to the coarse microstructure, which has characteristic dimensions comparable to the size of the hourglass S-N sample geometry; this permits only a small number of colonies to be sampled for any weak orientation. Bache and Evans[55] have recently pointed out the significance of such weak microstructural orientations, and the related stress redistribution between individual grains, in causing premature crack initiation in titanium alloys.

B. *Mode I Fatigue-Crack Propagation*

1. *Large-crack behavior*

The variation in (mode I) fatigue-crack growth rates for large (>4 mm) through-thickness cracks in the bimodal[30,31] and lamellar microstructures is shown in Figure 6 for constant-load-ratio tests at $R = 0.1$, 0.5, and 0.8. Corresponding average threshold values are listed in Table III. These results, which were collected at a frequency of 50 Hz, clearly show the expected trend of faster crack growth rates and lower ΔK_{TH} thresholds with increasing *R*-value. More importantly, in the coarser lamellar structure, growth rates were consistently lower, by roughly one order of magnitude at comparable ΔK levels, and thresholds higher, by more than 20 pct, at comparable load ratios, although there was considerably more scatter in the data for the lamellar microstructure. Specifically, between $R = 0.1$ and 0.8, (mode I) ΔK_{TH} thresholds varied, respectively, from 5.7 to 3.9 MPa$\sqrt{\text{m}}$ in the lamellar structure compared to 4.6 to 2.6 MPa$\sqrt{\text{m}}$ in the bimodal structure; corresponding two-parameter fits of the growth rates in the Paris regime give (in units of m/cycle, MPa$\sqrt{\text{m}}$):

$$\frac{da}{dN} = 5.2 \times 10^{-12} \Delta K^{2.5} K_{\max}^{0.67} \qquad \text{(bimodal structure)}$$

$$\frac{da}{dN} = 1.25 \times 10^{-14} \Delta K^{4.5} K_{\max}^{0.67} \qquad \text{(lamellar structure)}$$

The variation in the fatigue thresholds, plotted as the ΔK_{TH} threshold as a function of the $K_{\max,TH}$ threshold, is shown in Figure 7 for a wider range of *R*-ratios up to 0.98, the latter results being obtained using constant-$K_{\max}$ tests conducted at high values of $K_{\max}$. It is apparent that neither structure showed evidence of the Marci effect,[56] where near-threshold growth rates start to *increase* with decreasing ΔK levels at very high load ratios, most probably due to the superposition of a sustained-load (*e.g.*, environmentally induced) cracking mechanism. Indeed, at these extremely high $K_{\max}$ values, essentially as $K_{\max} \rightarrow K_{Ic}$ ($R \rightarrow 1$), the difference in ΔK_{TH} thresholds between the two structures is lost, with both microstructural conditions showing a so-called "*worst-case*" ΔK_{TH} threshold of 1.9 MPa$\sqrt{\text{m}}$.*

*The worst-case threshold[30] is a term given to the lowest value of ΔK_{TH} measured with large cracks at load ratios that approach unity (specifically, where $K_{\max} \rightarrow K_{Ic}$), such that the extent of crack-tip shielding, *e.g.*, by

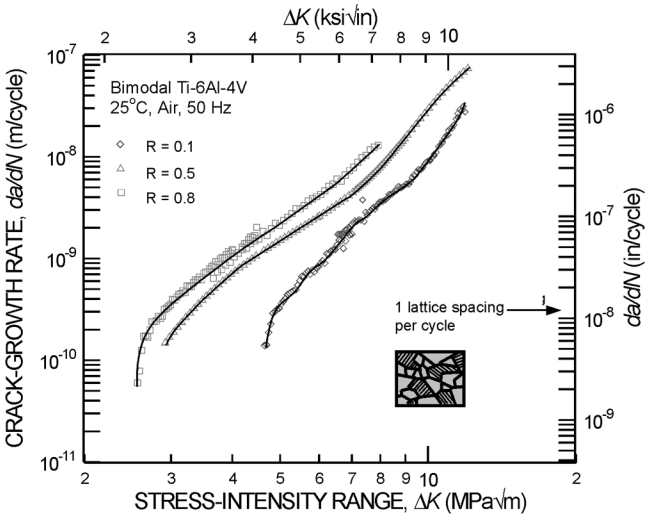

(*a*)

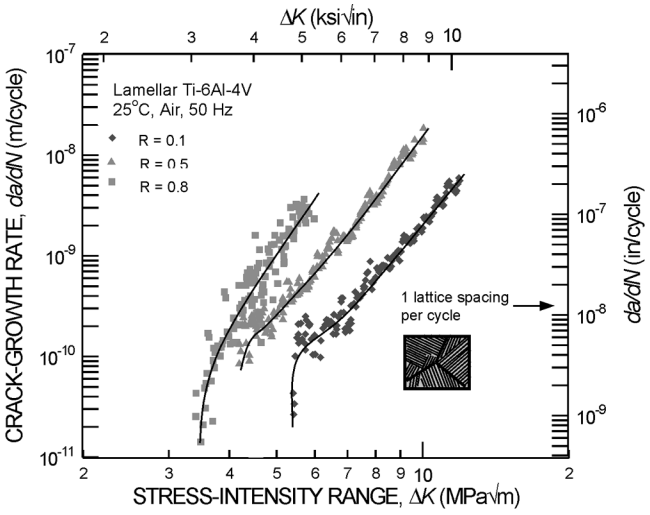

(*b*)

Fig. 6—Mode I fatigue-crack propagation (large crack) behavior of (*a*) bimodal Ti-6Al-4V in terms of the crack-growth rates, *da*/*dN*, as a function of the applied stress-intensity range, ΔK, at various load ratios (R = 0.1, 0.5 and 0.8), all at a frequency of 50 Hz. Fatigue thresholds measured at $da/dN = 1 \times 10^{-10}$ m/cycle were 4.6, 3.6, and 2.9 MPa$\sqrt{\text{m}}$, respectively.[30,31] (*b*) For the lamellar microstructure, fatigue thresholds measured at $da/dN = 1 \times 10^{-10}$ m/cycle were 5.7, 4.4, and 3.9 MPa$\sqrt{\text{m}}$, respectively.

crack closure, is minimized. Such thresholds, which are generally measured under constant-K_{max}/increasing-K_{min} cycling, represent a lower-bound threshold for the alloy/microstructure in question in the presence of "continuum-sized" cracks, *i.e.*, in the presence of physically large or small cracks which have dimensions specifically larger than the characteristic scale of the microstructure.

It should be noted that although the data shown in Figure 6 were collected at a loading frequency of 50 Hz, the growth-rate behavior of the bimodal microstructure over the range from 50 to 20,000 Hz and of the lamellar microstructure between 50 and 1000 Hz was examined. In ambient-temperature air, no effect of frequency on the (mode I) ΔK_{TH} thresholds was seen in either microstructure.[30,31,34] Previous investigations have reported frequency-independent growth rates for titanium alloys in the 0.1 to 50 Hz range;[57,58] the current results significantly extend these observations.

Thus, the lamellar structure clearly provides superior

Table III. Average Threshold Values for Ti-6Al-4V

	Bimodal Microstructure		Lamellar Microstructure	
Load Ratio R	ΔK_{TH} (MPa$\sqrt{\text{m}}$)	$K_{max,TH}$ (MPa$\sqrt{\text{m}}$)	ΔK_{TH} (MPa$\sqrt{\text{m}}$)	$K_{max,TH}$ (MPa$\sqrt{\text{m}}$)
0.10*	4.3	4.8	5.7	6.3
0.30*	3.6	5.2	5.0	7.1
0.50*	2.9	5.9	4.4	8.8
0.80*	2.5	12.5	3.9	19.5
0.88**	—	—	3.2	26.5
0.91**	2.3	26.5	—	—
0.92**	—	—	3.0	36.5
0.94**	2.2	36.5	2.8	46.5
0.952**	—	—	2.7	56.5
0.955**	2.1	46.5	—	—
0.965**	2.0	56.5	2.4	66.5
0.973**	—	—	2.0	76.5
0.978**	—	—	1.9	86.5

*Determined under constant R conditions.
**Determined under constant K_{max} conditions.

mode I fatigue-crack-propagation resistance to the bimodal structure *in the large-crack regime*, an observation that can primarily be traced to the increased tortuosity in the crack path and resulting crack closure in the lamellar structure, as discussed in Section IV-B-3. However, this beneficial aspect of the lamellar structure is progressively diminished with increasing load ratio, again consistent with the diminishing role of crack closure, such that for $R > 0.8$, ΔK_{TH} thresholds in the two microstructures are essentially the same.

2. *Crack closure*

Crack-tip shielding from crack closure in titanium alloys has been primarily attributed to the roughness of the crack surfaces, *i.e.*, to the wedging of crack-face asperities; indeed, load-ratio effects in these alloys are generally presumed to result from such closure.[59,60,61] In the present study, significant closure was observed at the low R-ratios of 0.1 and 0.3 for both microstructures; none could be detected at $R \geq 0.8$. The magnitude of such closure, in terms of the variation in K_{cl}, and, hence ΔK_{eff}, with ΔK is shown in Figure 8. Unlike the bimodal structure, closure levels in the lamellar structure can be seen to vary with ΔK level at low growth rates, consistent with previous studies.[60] However, more importantly, the overall magnitude of the closure effect is definitively higher in the coarser lamellar structure. As discussed in Section IV-B-3, this undoubtedly results from the increased tortuosity in the crack path and, hence, in the fracture-surface roughness associated with this microstructure.

3. *Crack-path and fracture-surface morphologies*

As shown in Figure 9, the coarser lamellar microstructure displayed a more tortuous and deflected crack path than the finer-scale bimodal microstructure. Whereas the controlling microstructural unit in the bimodal structure is the grain size, which is ~20 μm, it is clearly the entire lamellar colony size in the lamellar structure, which is more than one order of magnitude larger; furthermore, the deflection of the crack path across such boundaries in the latter structure can be seen to be strongly influenced by the orientation of neighboring colonies. Such increased crack-path tortuosity is a major contributor to the higher toughness of the lamellar microstructure.[8] Moreover, as noted previously, the enhanced

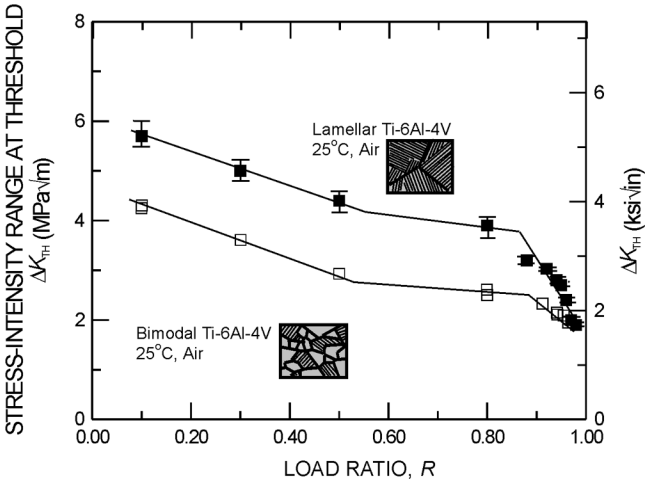

(*a*)

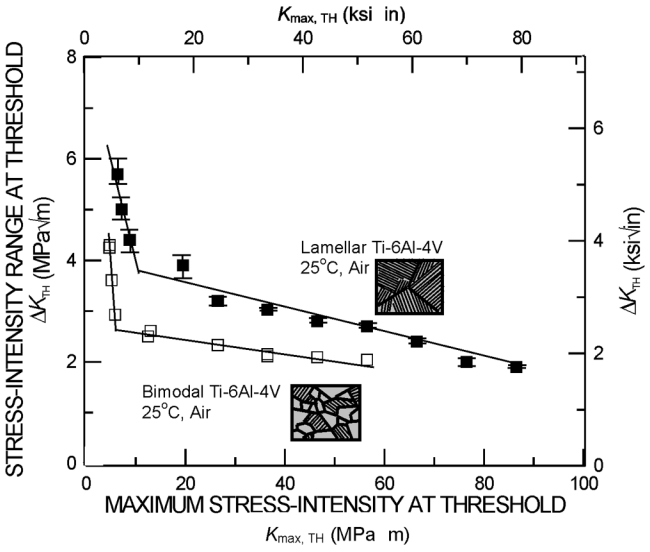

(*b*)

Fig. 7—(*a*) The mode I large-crack ΔK_{TH} thresholds obtained for both bimodal and lamellar microstructures are shown as a function of the load ratio, *R*. The data include both constant-*R* and constant-K_{max} test results. At very high *R*-ratios (>0.9), ΔK_{TH} thresholds for both microstructures tend to converge. (*b*) The same data are plotted as a function of the K_{max} at threshold.

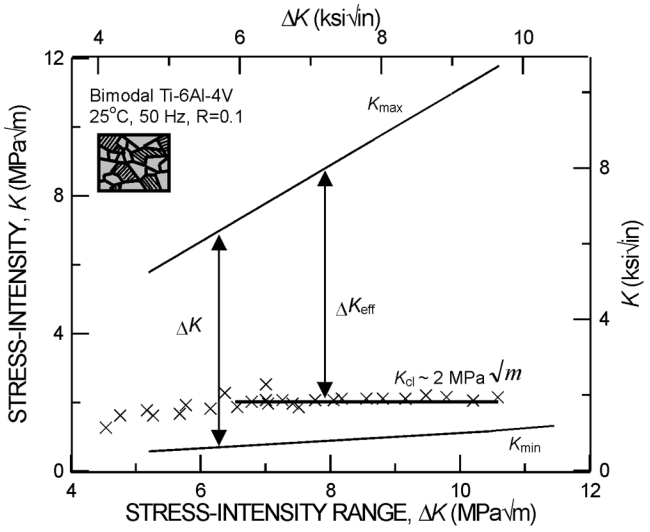

(*a*)

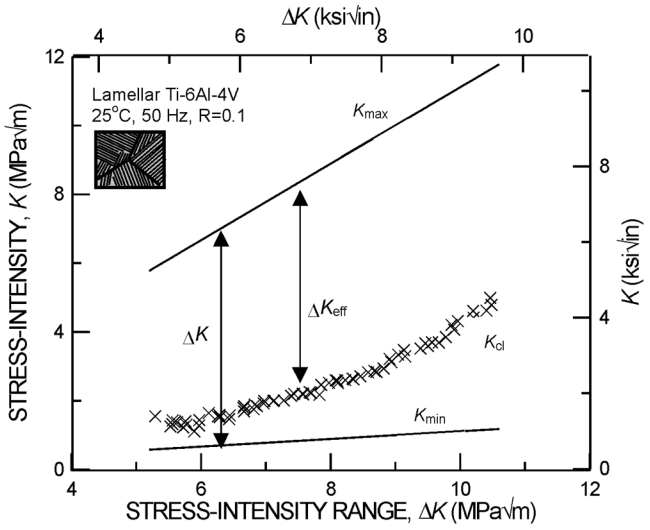

(*b*)

Fig. 8—Crack closure, measured at $R = 0.1$, using unloading compliance techniques on *C*(*T*) specimens for the (*a*) bimodal and (*b*) lamellar microstructures.

crack deflection and resulting roughness-induced crack closure both act to increase the fatigue-crack-growth resistance of this structure *in the presence of large cracks* and to increase the degree of scatter in the crack-growth data (Figure 6). At high *R*-values, where both microstructures show a decrease in such tortuosity, the difference between the cyclic crack-growth resistance of the two structures becomes essentially nonexistent. The less-deflected crack paths here may be associated with the much larger maximum plastic zone sizes as $K_{max} \rightarrow K_{Ic}$ ($R \rightarrow 1$); this markedly increases the number of slip systems available, which can change single-slip planar crack growth (in the form of deflected, crystallographic, crack paths) to multiple-slip crack growth (where the crack path is more straight).

The more tortuous crack path in the lamellar structure results in a far-rougher fracture surface, as shown by the scanning electron micrographs in Figures 10 and 11 for the bimodal and lamellar structures, respectively, at load ratios of 0.1, 0.5, and >0.9. The ΔK levels associated with the fracture surfaces are ~4.3, 2.9, and 1.9 MPa$\sqrt{m}$, respectively, at $R = 0.1$, 0.5, and 0.96 for the bimodal structure (Figure 10) and ~5.7, 4.4, and 3.0 MPa$\sqrt{m}$, respectively, at $R = 0.1$, 0.5, and 0.92 for the lamellar microstructure (Figure 11). The highly crystallographic nature of the crack paths in the lamellar structure is particularly evident in Figure 11. Also shown is the overload fracture region for both microstructures, which occurs by microvoid coalescence.

4. *Short-crack behavior*

(Mode I) ΔK_{TH} thresholds for short cracks, where the crack wakes have been machined away to within ~200 μm of the crack tip, are compared with the large-crack thresholds as a function of *R* in Figure 12. Whereas large- and short-crack thresholds are essentially identical above approximately $R = 0.5$, at lower load ratios where crack closure

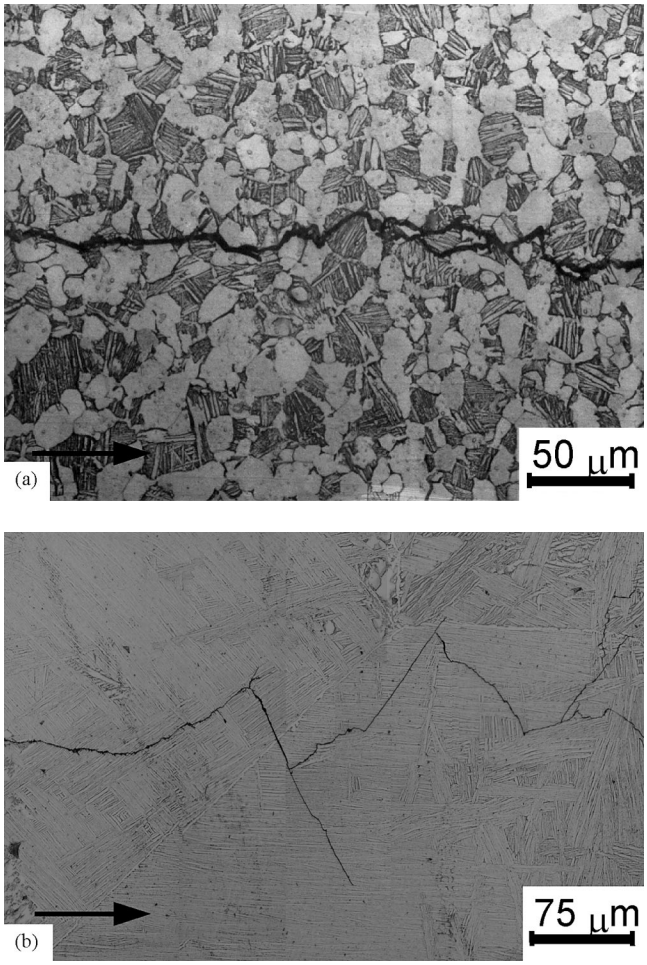

Fig. 9—A typical near-threshold crack profile observed for the (*a*) bimodal and (*b*) lamellar microstructure ($R = 0.1$, and $da/dN \sim 10^{-10}$ m/cycle). The nominal crack propagation direction is indicated by the arrow. The structure-sensitivity of fatigue-crack growth is clearly stronger for the lamellar microstructure.

was observed, thresholds are much smaller for the short cracks due to the restricted role of such closure for cracks of limited wake. Indeed, by correcting the large-crack ΔK_{TH} thresholds for closure, in the form of $\Delta K_{TH,\text{eff}}$ thresholds, threshold values for large and short cracks are the same, similar to previous observations in Ti-6A1-4V.[62]

5. *Small-crack behavior*

The fatigue-crack propagation behavior (at $R = 0.1$) of the microstructurally small surface cracks, where crack sizes were in the range of ~1 to 50 μm, are plotted as a function of both ΔK and surface-crack length, $2c$, for both microstructures in Figure 13; results are compared with corresponding data for through-thickness large (>4 mm) cracks at both $R = 0.1$ (from constant-R testing) and $R = 0.91$ to 0.95 (from constant-$K_{\max}$ testing). Several points are worthy of note:

(1) Growth rates for the microstructurally small cracks were, in general, far in excess of those of corresponding large cracks at equivalent ΔK levels. In both structures, the smallest cracks, with dimensions in the range ~2 to 20 μm, propagated at stress intensities well below the worst-case ("closure-free") thresholds for large cracks. Indeed, thresholds for such small cracks were below $\Delta K \sim 1$ MPa$\sqrt{\text{m}}$, presumably due to biased sampling by the small flaw of the "weak links" in the microstructure.

(2) With increasing crack size, growth rates for the small cracks merge first with the high-R (closure-free) large-crack data (at $2c \sim 50$ to 100 μm) and eventually with the low-R data at larger crack sizes.

(3) Although the lamellar structure shows superior fatigue-crack-growth properties in the presence of large ("continuum-sized") cracks (Figure 6), in the presence of the microstructurally small cracks, the fatigue-crack-growth resistance of the two structures is very similar, although the data are subject to considerably more scatter. This implies, though, that a primary difference in the fatigue-crack-growth properties of the bimodal and lamellar microstructures arises more from the extrinsic role of crack-path tortuosity and resultant crack closure, rather than any distinction in their respective intrinsic resistance to cyclic crack growth. Similar effects have been observed for other material systems (*e.g.*, Reference 63).

From the perspective of defining thresholds for HCF, however, the results in Figure 13 clearly demonstrate that the concept of a worst-case threshold (determined under $R \rightarrow 1$ conditions that minimize crack closure) applies strictly for continuum-sized cracks; such thresholds do not provide a lower-bound threshold stress intensity for cracks on the scale of microstructural dimensions. As discussed in Section IV–D, this is particularly pertinent for the early stages of FOD-induced fatigue failures.

It is interesting to note that the small-crack growth rates do not vary that much with microstructure, whereas the crack initiation mechanisms are strongly influenced by microstructure, as noted previously. Such initiation is often controlled by strain accumulation at the tips of the longest slip band, which leads to preferential nucleation and initial growth within the interconnected primary α grains in the bimodal microstructure. In the lamellar microstructure, cross-colony slip-band crack initiation is observed, with subsequent small-crack growth generally occurring along the planar-slip bands into adjoining, but differently oriented, colonies. The coarser microstructure provides a longer path for the small crack to propagate before it encounters a serious microstructural "barrier" such as differently oriented neighboring colonies.

Thus, in general, whereas the lamellar structure offers better resistance to large-crack fatigue-crack growth than the bimodal structure, there is little difference in the resistance of the two microstructures to small-crack growth.

C. *Mixed-Mode Fatigue Thresholds*

1. *Large-crack behavior*

Results for the large-crack threshold behavior of the bimodal and lamellar microstructures under mode I + II loading are shown in Figure 14 in the form of mixed-mode threshold envelopes, where the mode II threshold stress-intensity range ($\Delta K_{\text{II},TH}$) is plotted as a function of the corresponding mode I threshold ($\Delta K_{\text{I},TH}$). Once more, several points are worthy of note:

(1) Similar to the behavior in other materials,[64–67] a clear reduction in threshold values with increasing R-value is evident. The slight increase in the $\Delta K_{\text{I},TH}$ threshold with increasing mode-mixity at low phase angles, observed

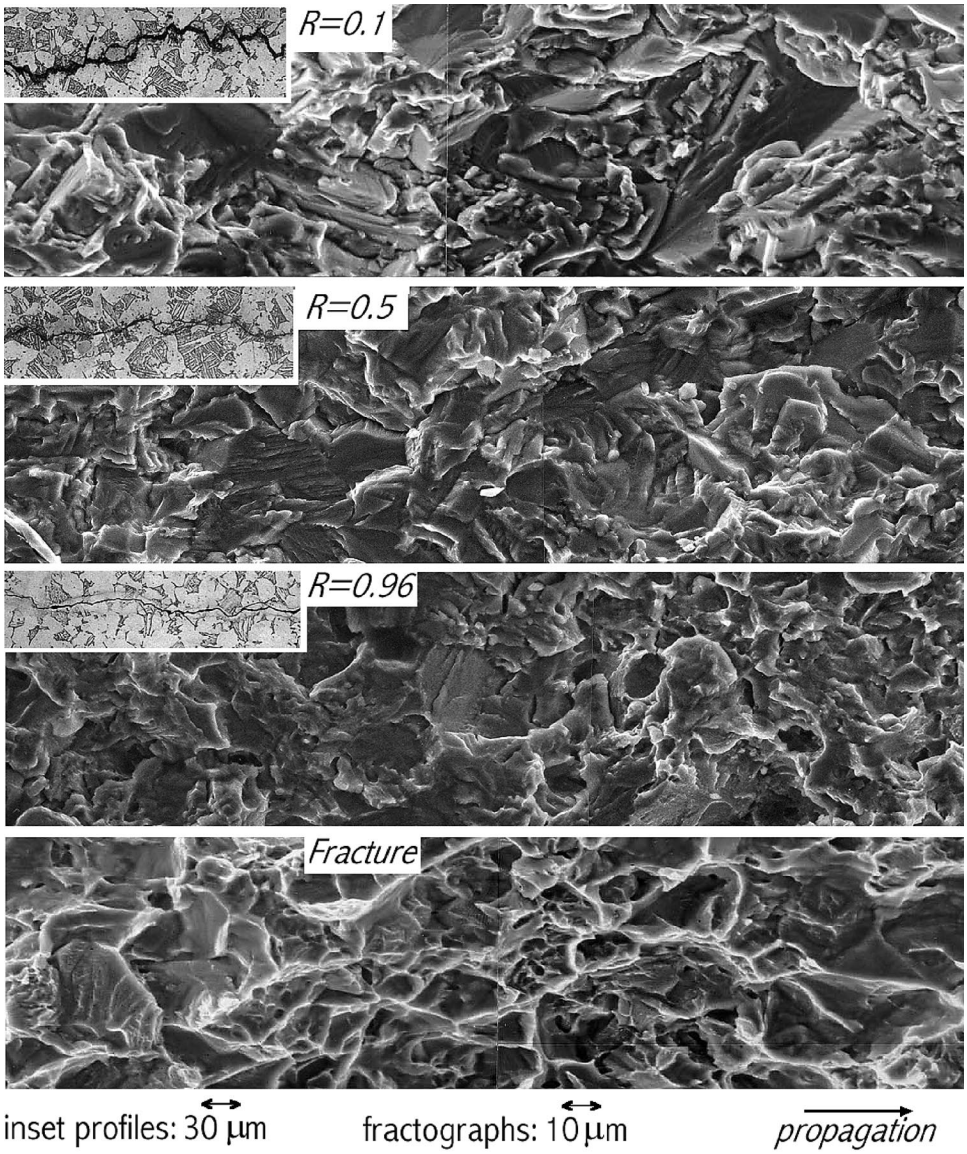

Fig. 10—A comparison of the fractography and crack profiles (inset) observed at near-threshold growth rates of $\sim 10^{-10}$ m/cycle in the bimodal microstructure. Whereas microvoid coalescence can be seen in overload fracture, no such static modes are evident in fatigue, even at $R = 0.96$.

in the present data at phase angles between 0 and 26 deg, has been attributed to an effect of mode I/mode II crack-tip shielding.[43,44].

(2) Although the mode I threshold decreases with increasing mode-mixity, if a more appropriate measure of the mixed-mode driving force is used, specifically the range in strain-energy release rate ($\Delta G = (\Delta K_I^2 + \Delta K_{II}^2)/E'$, where $E' = E$ (Young's modulus) in plane stress and $E/(1 - \nu^2)$ in plane strain (ν being the Poisson's ratio), then there is a progressive increase in the mixed-mode threshold (ΔG_{TH}) with increasing mode-mixity in both microstructures for all load ratios studied (Figure 15). From the perspective of thresholds for high-cycle fatigue, this implies that, in terms of mixed-mode loading, the mode I threshold, defined in terms of ΔG, represents a *worst-case* condition. Naturally, this is also evident when the equivalent stress-intensity factor range, $\Delta K_{eq,TH} = (\Delta G_{TH} E')^{1/2}$, is used to characterize the threshold (Figure 15).

(3) As discussed in detail elsewhere,[43,44] the increase in the large-crack mixed-mode threshold with increasing mode-mixity can be related in these microstructures to an increased role in mode I and mode II crack-tip shielding, associated with, respectively, crack closure and sliding-crack interference (*i.e.*, friction and interlock of crack-surface asperities). Indeed, if such data are "corrected" for this shielding by characterizing the driving force in terms of a mixed-mode ΔG_{eff},[43] then the effect of the mode-mixity on the threshold is greatly reduced (shown by the hatched regions in Figure 16).*

*The term ΔG_{eff} is defined as $(\Delta K_{I,eff}^2 + \Delta K_{II,eff}^2)/E'$, where $\Delta K_{I,eff}$ is the effective stress-intensity range in mode I, and $\Delta K_{II,eff}$ is the corresponding effective stress-intensity range in mode II. The value of $\Delta K_{I,eff}$ is determined in the usual way, in terms of $K_{I,max} - K_{cI}$. The value of $\Delta K_{II,eff}$, on the other hand, is equal to the difference between the near-tip maximum and minimum mode II stress intensities in the fatigue cycle. The near-tip mode II stress-intensity range differs from the applied driving force due to the presence of shear-induced fracture-surface asperity contact and interlock.

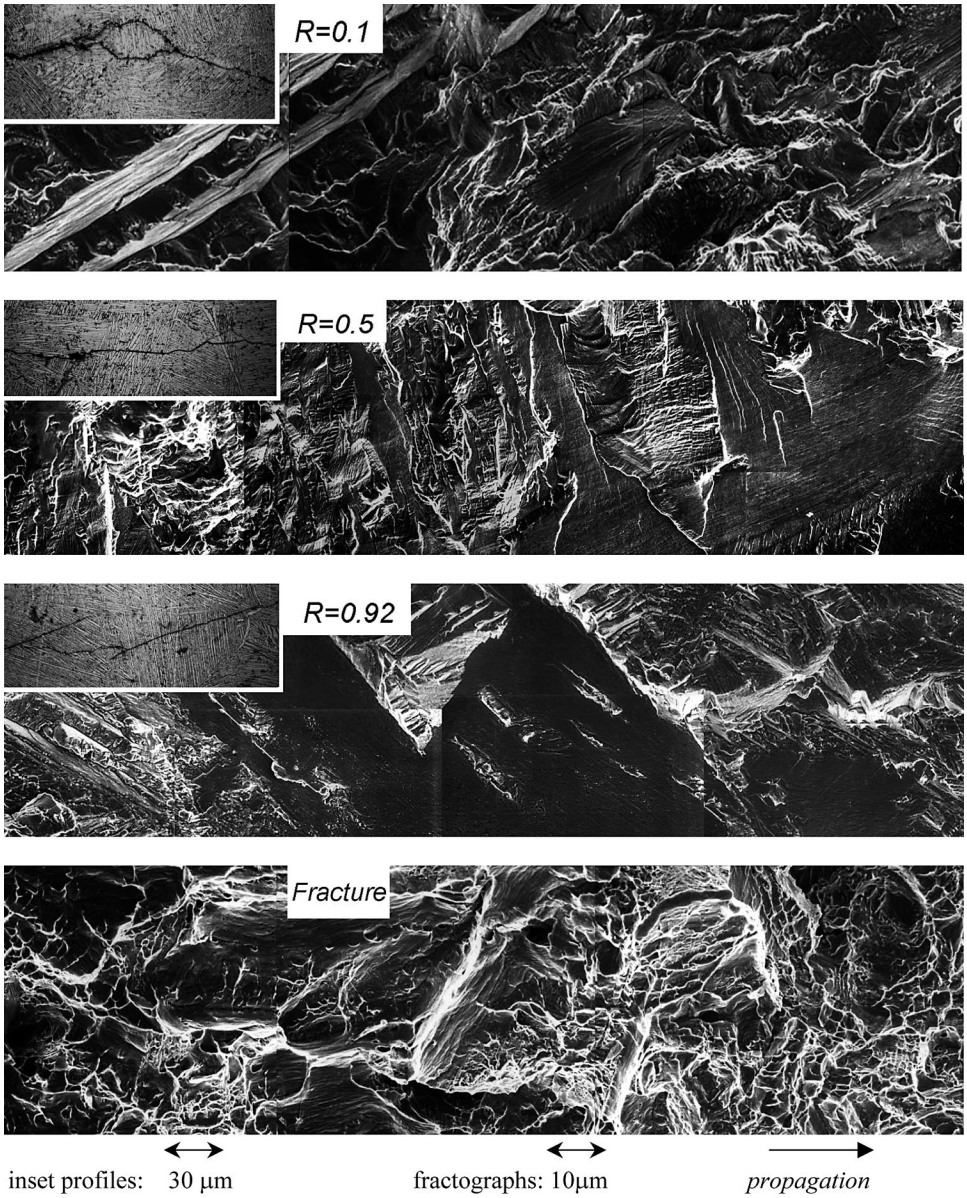

Fig. 11—A comparison of the fractography and crack profiles (inset) observed at near-threshold growth rates of $\sim 10^{-10}$ m/cycle in the lamellar microstructure. The lamellar microstructure generally exhibits greater crack path tortuosity and fracture surface roughness.

Further details on the determination of $\Delta K_{I,eff}$ and the estimation of $\Delta K_{II,eff}$ using compliance-based techniques can be found in Reference 44.

(The shielding correction was based on compliance-based measurements of the mode I crack closure and mode II crack-surface interference and is described in Reference 44). Similarly, as discussed subsequently for short and small cracks, where such shielding is highly diminished due to the restricted crack wake, the mixed-mode threshold shows very little sensitivity to the mode-mixity.

(4) Akin to pure mode I behavior, in the presence of large cracks, the lamellar structure displays superior mixed-mode crack-growth resistance to the bimodal structure. This is attributable to the large degree of crack deflection, bifurcation, and secondary crack formation associated with crack growth in the lamellar structure, as shown in Figure 17; all these factors result in rougher fracture surfaces which, under sliding conditions (even more so than with tensile opening), can significantly promote crack-tip shielding (by sliding crack-surface interference) in large cracks. This difference in crack-growth resistance between the microstructures is considerably reduced at phase angles approaching 90 deg, although the reason for this is, as yet, unclear.

2. *Short-crack behavior*

The mixed-mode thresholds for short ($\sim$200 μm) cracks in the bimodal and lamellar structures are plotted in Figure 16 as a function of the phase angle; results are compared with the corresponding thresholds for large cracks from Figure 15. As noted previously, the effect of crack-tip shielding in the crack wake is particularly significant in the presence of shear loading, due to crack-surface friction and interlocking of asperities.[44,66–70] Consequently, due to the minimal role of crack-tip shielding with cracks of limited wake, short-crack

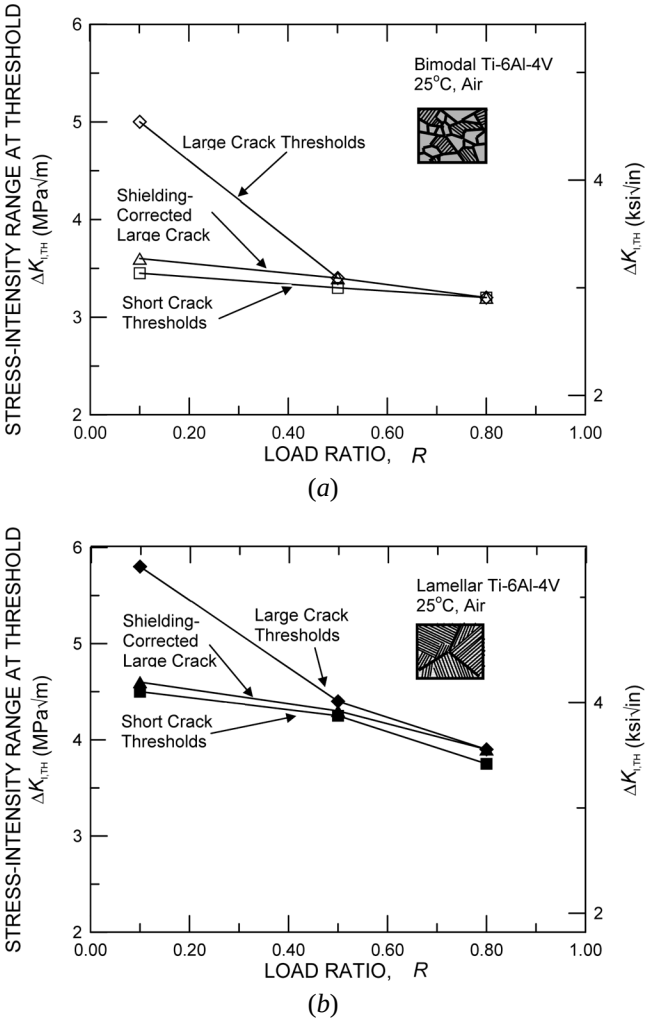

Fig. 12—(*a*) and (*b*) Mode I large-crack ΔK_{TH} threshold values obtained for the bimodal and lamellar microstructures using symmetric four-point bending tests are shown, together with the corresponding values "corrected" for crack closure. Thresholds for short (~200 μm) through-thickness cracks are also shown for reference.

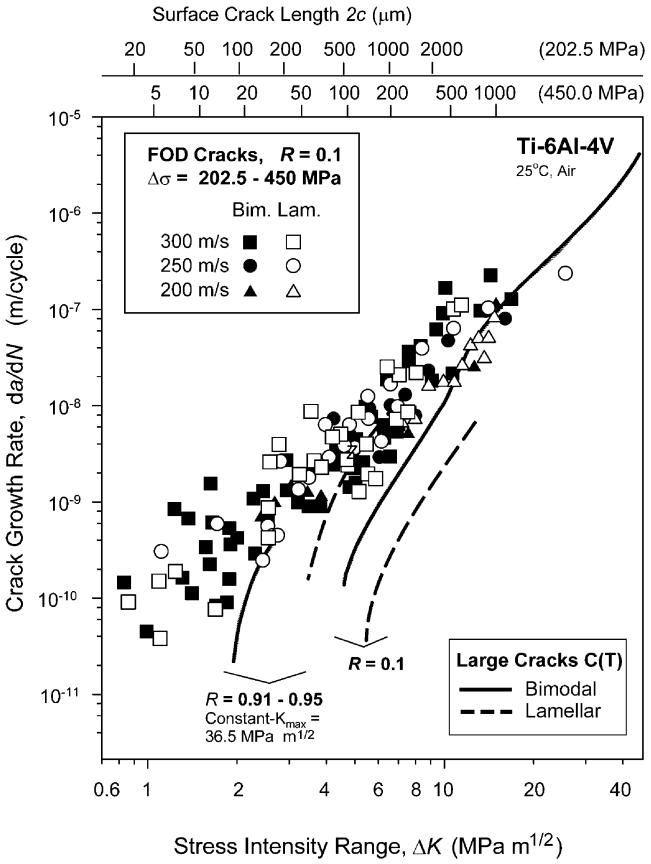

Fig. 13—Fatigue-crack growth rates as a function of applied stress-intensity range at $R = 0.1$ for FOD-induced small (~2 to 50 μm) surface cracks in the bimodal and lamellar microstructures. Large-crack growth data at $R = 0.1$ were obtained from constant load-ratio tests, whereas corresponding data at $R = 0.91$ to 0.95 were obtained using constant-K_{max}/increasing-K_{min} testing.

thresholds can be seen to be (1) far smaller than the large-crack values, (2) relatively insensitive to mode-mixity, in contrast to the large-crack thresholds, and (3) insensitive to the load ratio, again in contrast to large-crack results. Moreover, the short-crack threshold values were observed to lie within the scatter band for shielding-corrected large cracks,[43,44] again indicating that, similar to mode I conditions, the limited effect of shielding for short cracks is responsible for their lower threshold values. It should be noted here that, in addition to errors from varying precrack lengths, these tests (akin to large-crack tests[43]) are subject to errors caused by small variations in the offset of the crack from the load line of the AFPB geometry. The root-mean-square error in this offset has been determined to be 0.081 mm.[43] At a phase angle of 82 deg and a load ratio of 0.1, this translates into typical errors of $\sim\pm 2.6$ deg in β and $\sim\pm 2$ J/m^2 in the threshold values; such uncertainties in ΔG_{TH} values are typical for the entire range of R and β values studied.

With respect to microstructural effects, the distinction between the bimodal and lamellar microstructures in terms of the mixed-mode crack-growth resistance is substantially reduced for short cracks, compared to that for large cracks; however, the lamellar structure still displays somewhat higher ΔG_{TH} thresholds, particularly at the lower R-values.

3. *Small-crack behavior*

The results presented in Figure 16 show a marked effect of crack size on the mixed-mode thresholds, which we have attributed to a difference in the magnitude of the crack-tip shielding. However, even lower mixed-mode thresholds have been measured for microstructurally small (<50 μm) surface cracks, where there is the additional factor of the biased sampling of the weak links in the microstructure by the small flaw. As shown in Figure 18 for the bimodal structure, the large-crack ΔG_{TH} mixed-mode thresholds at $\Delta K_{II}/\Delta K_I = 7.1$ ($R = 0.1$) are some 70 to 90 times larger than such measured small-crack thresholds. As there is little to no information in the literature concerning the mixed-mode behavior of such small flaws, this would appear to be an important topic for further investigation.

D. *Thresholds for FOD*

High-velocity impacts of hardened steel spheres simulating FOD resulted in a dramatic reduction in the fatigue life in both microstructures, as shown by the *S-N* data in Figure 3. Lifetimes are reduced by a minimum of two orders of

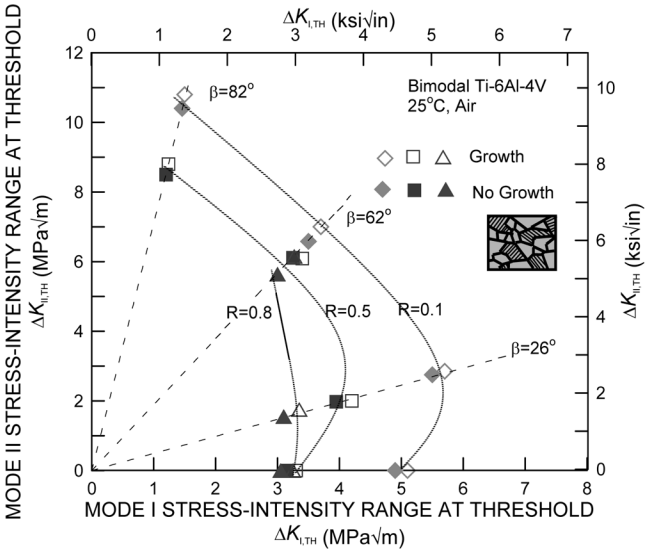

(*a*)

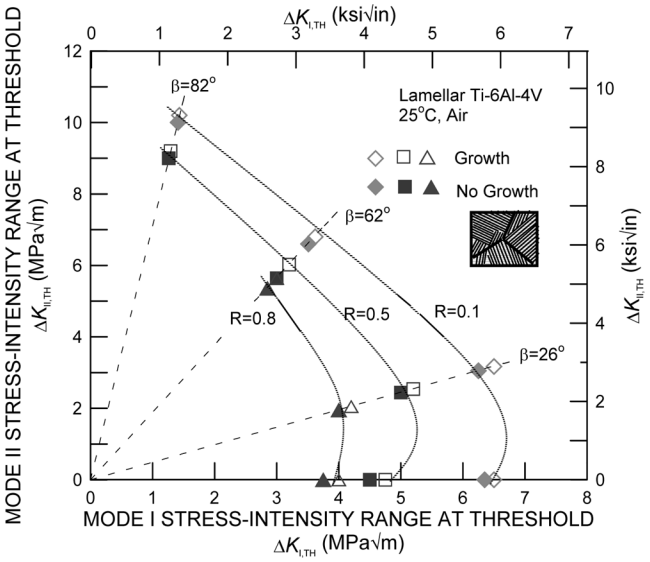

(*b*)

Fig. 14—Mixed-mode threshold envelopes for large (>4 mm) through-thickness cracks in the (*a*) bimodal and (*b*) lamellar microstructures. Note that the lamellar structure shows superior resistance to crack propagation, particularly at the lower phase angles.

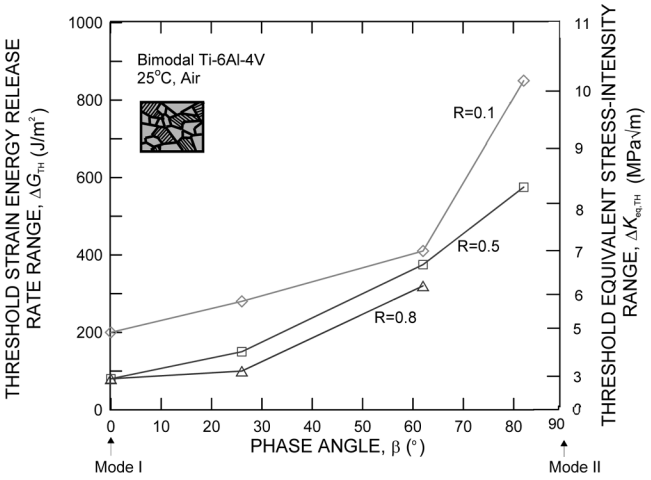

(*a*)

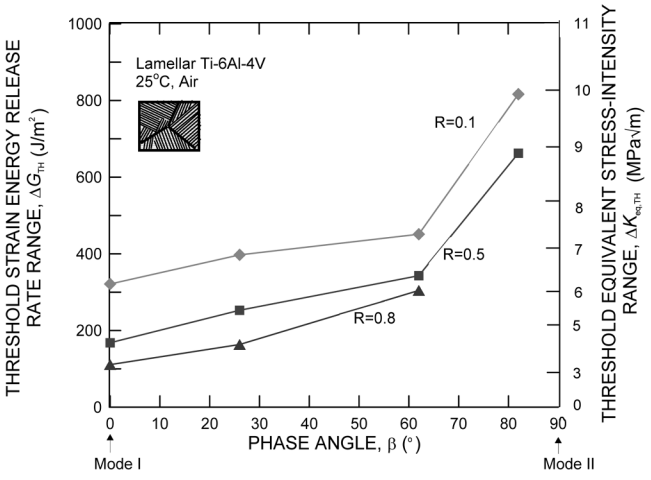

(*b*)

Fig. 15—The threshold strain-energy release rate, ΔG_{TH}, is plotted as a function of phase angle, β, for both microstructures for large cracks subjected to mixed-mode loading at $R = 0.1$, 0.5, and 0.8. Equivalent stress-intensity ranges at threshold for both microstructures are also shown. The lamellar microstructure generally displays superior resistance to fatigue-crack propagation.

magnitude, and FOD-induced failures can be seen to occur in as little as 2×10^4 cycles at stresses below the smooth-bar fatigue limit. Corresponding images of the typical damage sites, following 300 m/s impacts on the flat surface of the fatigue samples, are shown in Figure 19 for both microstructures.

As discussed in detail elsewhere,[40,47] the mechanistic effect of such FOD can be considered in terms of (1) the possibility of forming microcracks in the damage zone, (2) the stress concentration associated with the FOD-induced notches, (3) microstructural damage from FOD-induced plastic deformation, and (4) the localized presence of tensile residual hoop stresses in the vicinity of the impact site. Although all these factors play an important role, a pivotal effect of FOD in reducing fatigue life in Ti-6Al-4V appears to be the formation, at high impact velocities, of damage-induced microcracks; on subsequent cycling, these can act preferred sites for the premature initiation of fatigue cracks in the pileup of material around the rim of the impact crater, depending upon the relative magnitude of the residual stresses in the vicinity of the impact.[71] This pile-up of material at the crater rim can be seen in Figure 19; within this region, numerous microcracks (~1 to 50 μm in size) are formed, which (when favorably oriented to the applied stress axis) serve as the starting point for fatigue cracking during subsequent cycling. Moreover, circumferentially oriented intense shear bands are formed at the higher impact velocities; these emanate from the surface of the impact crater and can be seen as concentric rings on the surface of the crater. The development of the pileup of material at the crater rim and the presence of shear banding and microcracking was more severe for the lamellar microstructure; however, although the microcrack density was increased, the size of the individual microcracks (*i.e.*, ~2 to 50 μm) was comparable to that seen in the bimodal microstructure.[48]

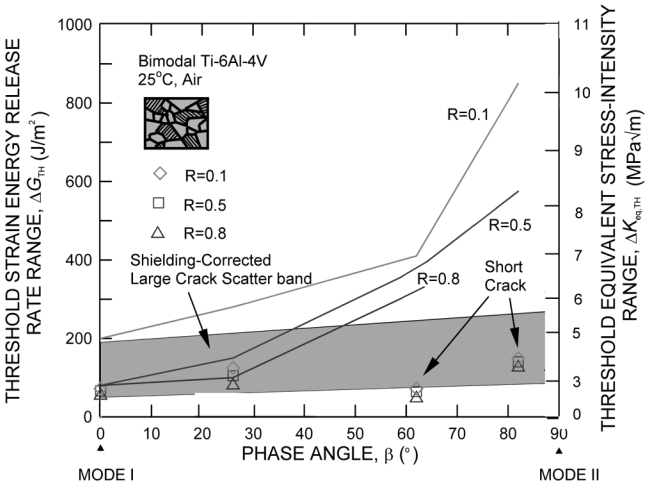

(*a*)

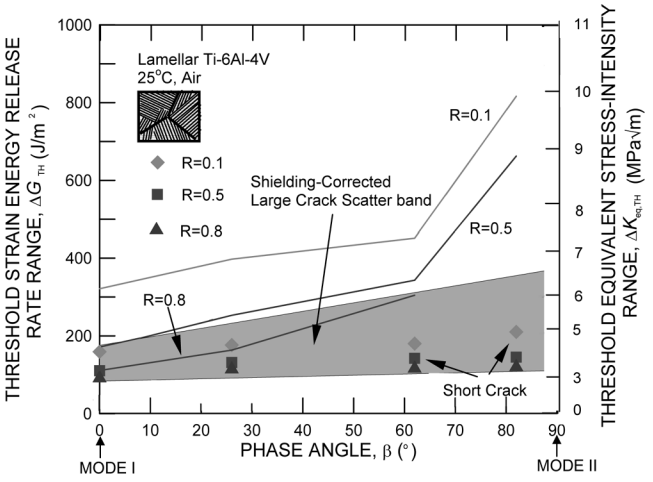

(*b*)

Fig. 16—Variation in mixed-mode thresholds, ΔG_{TH}, as a function of phase angle, β, in (*a*) and bimodal and (*b*) lamellar structures. Shown are results at three load ratios for large (>4 mm) cracks, before and after "correcting" for crack-tip shielding, and for short (~200 μm) through-thickness cracks.

The growth rates of the microstructurally small cracks that are initiated at, or near, such damage sites are shown in Figure 13. As discussed in Section IV–B–5, there is apparently little difference between the early growth of such FOD-initiated cracks in the two microstructures. However, it can be seen that the growth of <5-μm-sized microcracks commences at ΔK levels of ~1 MPa$\sqrt{\text{m}}$; as this is far below the worst-case thresholds for continuum-sized cracks, an alternative approach must be found to describe the threshold conditions for HCF in the presence of FOD.

In light of the vanishingly low thresholds for microstructurally small cracks in Ti-6Al-4V, an alternative approach to describe the threshold conditions HCF failures can be found using modified Kitawaga–Takahashi diagrams,[72] where the threshold-stress *range* for fatigue failure ($\Delta\sigma$) is plotted as a function of the surface-crack size, 2*c*, as shown in Figure 20. For the present case of FOD-initiated HCF, we have proposed coupling the worst-case threshold stress intensity with the 10^7-cycle smooth-bar fatigue limit to describe the HCF failure envelope, which is plotted for the bimodal and lamellar microstructures in Figures 20(a) and (b) at $R = 0.1$ and 0.5, respectively.[47]

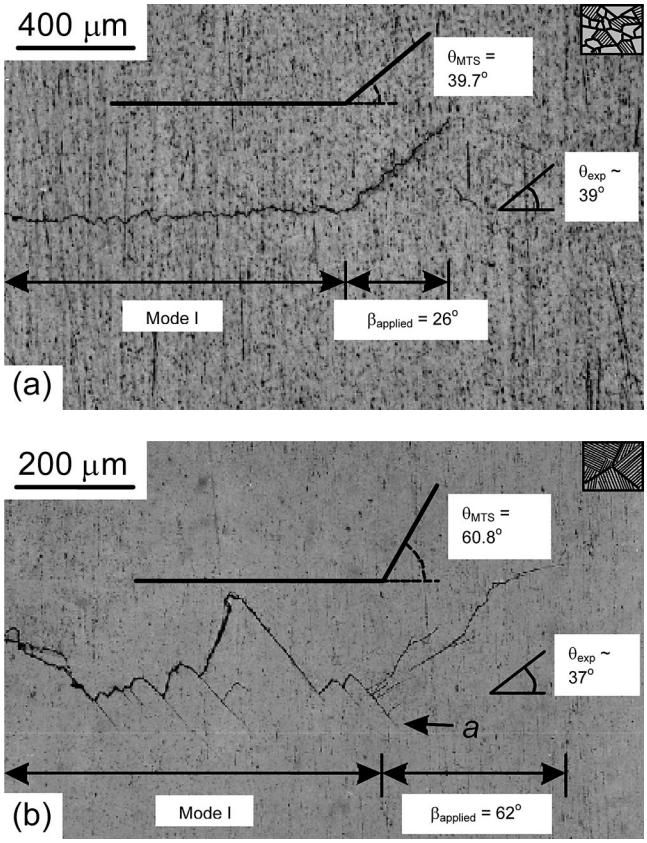

Fig. 17—Fatigue crack profiles are compared for the (*a*) bimodal (R = 0.8, and $\beta = 26$ deg) and (*b*) lamellar ($R = 0.1$, and $\beta = 62$ deg) microstructures. Optical micrographs show both the mode I fatigue precrack and the region of deflected crack growth following the application of cyclic mixed-mode loading. Measured crack deflection angles, θ_{exp}, are compared with those predicted by the path of maximum tangential stress, θ_{MTS} (References 43 and 44).

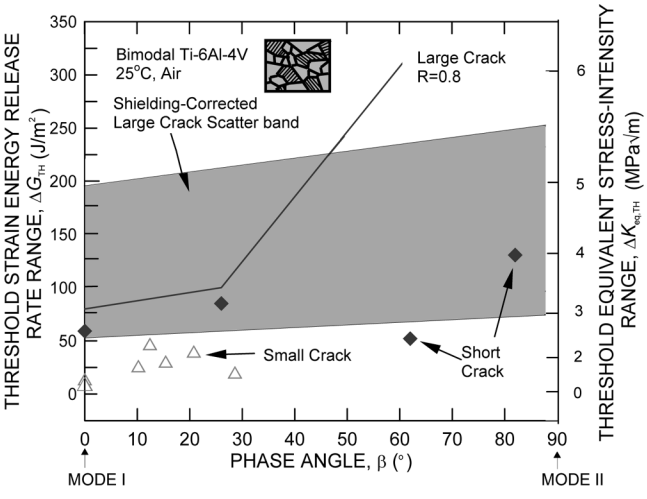

Fig. 18—Variation in mixed-mode thresholds, ΔG_{TH}, as a function of phase angle, β, for small (<50 μm) surface cracks in the bimodal microstructure. Shown for comparison are results for short (~200 μm) through-thickness cracks and for large (>4 mm) cracks under worst-case, high R conditions.

Results for the bimodal microstructure (closed symbols, solid lines) show that crack growth at both load ratios from FOD-induced microstructurally small cracks can be adequately described by the fatigue limit, corrected for the stress

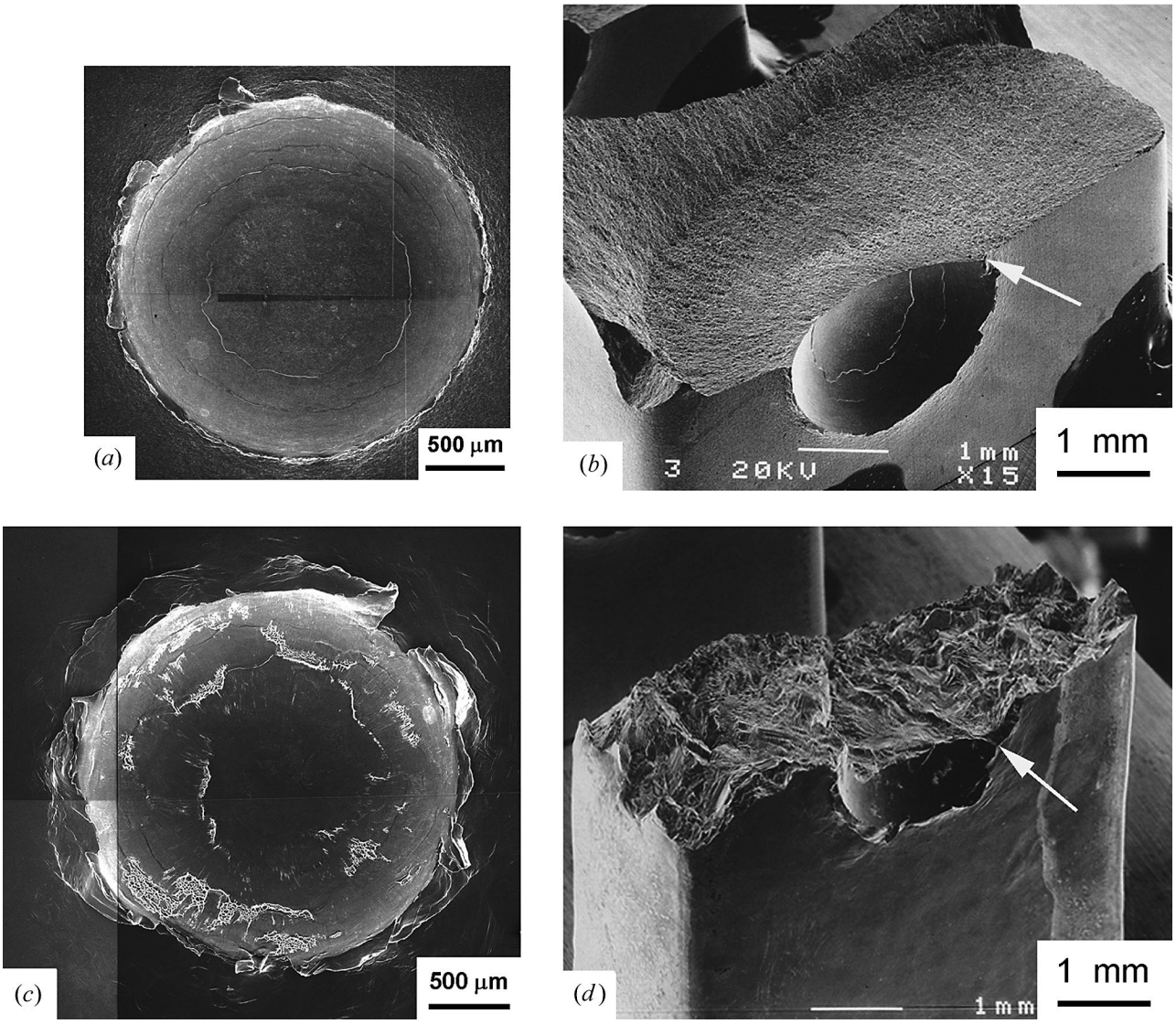

Fig. 19—FOD-induced craters formed following high velocity (300 m/s) impacts in the (*a*) bimodal and (*c*) lamellar microstructures. Note the extensive pileup observed at the impact crater rim, particularly for the lamellar microstructure. Failures initiated from impact-induced cracks at the crater rim (marked by arrows) in the (*b*) bimodal microstructure (nominally applied σ_{max} = 500 MPa, R = 0.1, and N_F = 65,000 cycles) and (*d*) lamellar microstructure (nominally applied σ_{max} = 500 MPa, R = 0.1, and N_F = 23,000 cycles).

concentration of the FOD indent, at small crack sizes, and the worst-case threshold stress intensity at larger continuum-sized crack sizes.* The failure envelopes in Figure 20 can be somewhat better represented by the El Haddad *et al.*[73] empirical quantification of the Kitagawa–Takahashi diagram, as shown. This approach introduces a constant, termed the "intrinsic crack size."* ($2c_0$), such that the stress intensity is defined as $\Delta K = Y\Delta\sigma\,(\pi(2c + 2c_0)^{1/2}$, where Y is the geometry factor.

With respect to the lamellar microstructure, shown by the open symbols and dashed lines in Figure 20, the Kitagawa–Takahashi approach is less suited. This structure does possess significantly better resistance to large-crack growth in the form of higher fatigue thresholds, and it possesses higher resistance to crack initiation in the form of a higher smooth-bar fatigue limit; however, it is more prone to the formation of FOD-induced microcracks, and such microstructurally small cracks exhibit a low resistance to propagation, even at stress-concentration-corrected stress ranges well below the fatigue limit.

*An additional correction is required for the case of low applied stresses (relative to the magnitude of residual tensile stresses in the vicinity of the damage sites (~300 MPa)). As described in detail elsewhere,[71] the effective load ratio in the Kitagawa–Takahashi plots needs to be corrected by superimposing the tensile residual stress as a mean stress. This approach is often unnecessary for higher applied stresses, due to relaxation of the residual stresses at the base and rim of the damage sites during initial fatigue cycling.[41]

*Although called the intrinsic crack size, this term is a fitting parameter and has no physical significance.

V. CONCLUDING REMARKS

The selection of an ideal microstructure for optimal HCF properties in an alloy represents a complex task, particularly

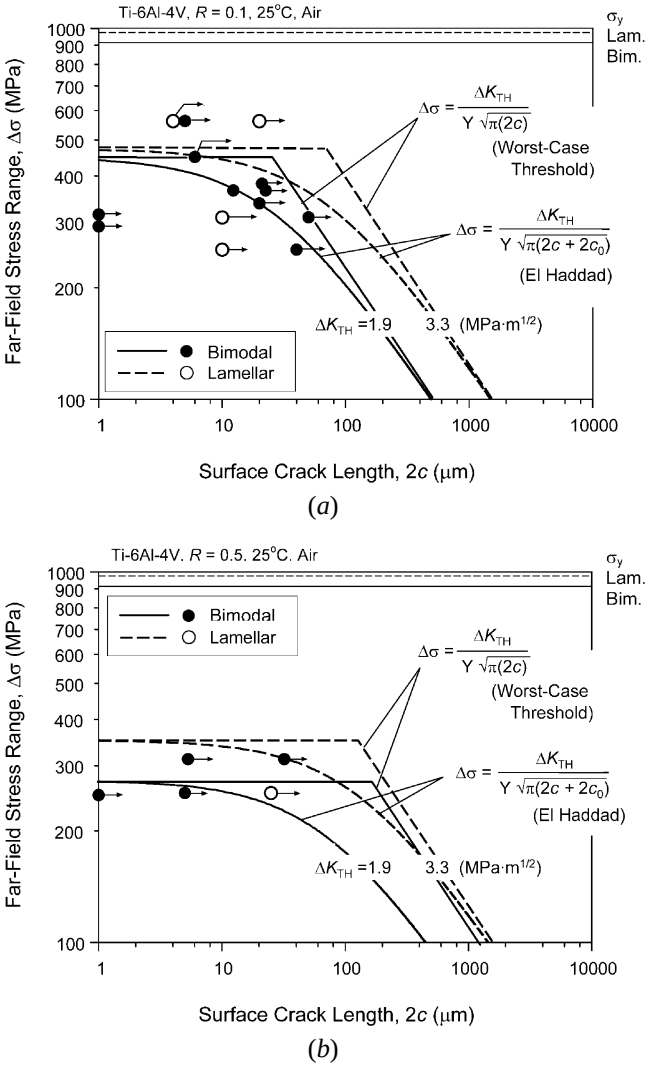

Fig. 20—Modified Kitagawa–Takahashi diagrams representing the threshold crack-growth conditions ($da/dN = 10^{-10}$ to 10^{-11} m/cycle) at (*a*) $R = 0.1$ and (*b*) $R = 0.5$ for FOD-induced small cracks in bimodal and lamellar Ti-6Al-4V. The threshold stress range as a function of the surface crack length is plotted, with the limiting conditions of the worst-case thresholds stress-intensity range at large crack lengths and the stress-concentration corrected 10^7-cycle smooth-bar fatigue limit at small crack lengths.

in view of the conflicting requirements of developing a high resistance to large-crack growth, which is generally referred to as the *damage tolerance*, together with similar resistance to crack initiation and small-crack growth, which generally determines the *durability*. Whereas large-crack growth resistance is often controlled by extrinsic factors, such as crack closure, which generally are promoted by coarse microstructures, resistance to crack initiation and small-crack growth is more of an intrinsic property of the microstructure and is promoted by finer-scale microstructures.

In the present case of Ti-6Al-4V alloys for turbine engine applications, the coarse β-annealed lamellar structure, which has a characteristic microstructural dimension over one order of magnitude larger than the equiaxed bimodal (STOA) structure, clearly has the better damage tolerance. It is a higher-strength, higher-toughness microstructural condition that develops higher levels of crack-tip shielding in both mode I and mode II from its more deflected crack paths and resulting rougher fracture surfaces; correspondingly, its large-crack fatigue-crack growth properties, in terms of mode I and mixed-mode fatigue thresholds, are definitely superior to those for the bimodal microstructure. However, at high load ratios where the effect of such shielding is diminished, the finer bimodal microstructure has comparable properties. Similarly, for the growth of microstructurally small cracks, specifically following FOD, again, where the role of shielding is minimized, the HCF resistance of the two microstructures is comparable. The problem with the lamellar structure is that it has a factor-of-4 lower ductility and, thus, is more prone to the formation of microcracks following impact damage. More importantly, cracks as large as $\sim$500 μm (the average colony size) may be considered as microstructurally small in the lamellar condition. As such cracks are prone to biased sampling of the microstructure, properties are subject to more scatter and often do not conform to measurements from larger samples, which reflect continuum behavior. Consequently, it may be much more difficult in practice to define *reliable* HCF threshold properties in the lamellar microstructure that will prevent the occurrence of HCF failures in service. A probabilistic framework for such modeling and predictions may be required in these instances.

VI. CONCLUSIONS

Based on a comparative study of the HCF properties of fine bimodal and coarse lamellar microstructures in Ti-6Al-4V, involving S-N behavior, mode I fatigue-crack propagation, and threshold behavior (as a function of load ratio and frequency) for large and small cracks, the corresponding fatigue-threshold behavior for large and small cracks under mixed-mode loading, and the role of FOD, the following conclusions can be made.

1. Although the differences are not large, the lamellar microstructure appears to display superior smooth-bar S-N cycle fatigue properties for lifetimes from $\sim 10^5$ to $> 10^8$ cycles at load ratios of 0.1 and 0.5, due to its roughly 10 pct higher tensile strength and coarser microstructural dimensions (which limited the number of colonies to be sampled for weak orientations). In contrast, at shorter lifetimes in the low-cycle regime, the bimodal microstructure exhibits the slightly better fatigue properties, presumably because of the much higher ductility of this microstructure.
2. Similarly, the lamellar microstructure displayed better (mode I) fatigue-crack-propagation properties than the bimodal microstructure in the presence of large (>4 mm) cracks. This was associated with the more tortuous crack paths in the coarser microstructure, which promoted higher levels of crack-tip shielding primarily by roughness-induced crack closure. Consequently, at high load ratios where the effect of such closure was minimal, the HCF threshold properties of the two microstructures were comparable. Indeed, worst-case mode I thresholds, defined at constant-K_{max}/increasing-K_{min} conditions to give very high load ratios ($R > 0.92$) and, hence, minimize the role of closure, were found to be 1.9 MPa$\sqrt{\text{m}}$ in both microstructures; these values can be regarded as lower-bound HCF threshold values for continuum-sized cracks.

3. In the presence of microstructurally small (~2 to 50 μm) cracks, as, for example, are formed following high-velocity impact damage, thresholds for fatigue-crack propagation were observed to be far less than the worst-case thresholds and approach ~1 MPa$\sqrt{\text{m}}$. The behavior in this regime was similar in both microstructures.
4. Mixed-mode large-crack measurements for both microstructures indicate that mixed-mode thresholds, characterized in terms of the strain-energy release rate, ΔG_{TH}, or the equivalent stress intensity, $\Delta K_{eq,TH}$, are increased with increasing mode-mixity; correspondingly, pure mode I ΔG_{TH} thresholds can be used as a conservative *worst-case* estimate. The larger threshold values with increasing mode-mixity can be attributed to an increased role of crack-tip shielding in mode I (crack closure) and mode II (crack-surface interference).
5. The lamellar microstructure displayed superior resistance to mixed-mode fatigue-crack propagation in the presence of large cracks; at very high mode-mixities, approaching pure mode II conditions (β = 82 deg), however, the properties of the bimodal and lamellar microstructure were similar.
6. Due to the limited effect of such shielding, mixed-mode thresholds for short (~200 μm) through-thickness and small (2 to 50 μm) surface cracks were found to be substantially less than the large-crack values and to be essentially insensitive to the mode-mixity. Short-crack thresholds were seen to be comparable to the large-crack threshold values after correcting for crack-tip shielding. The lamellar microstructure exhibited somewhat higher short-crack thresholds compared to the bimodal microstructure.
7. The FOD simulated by high-velocity impacts by hardened steel shot, was found to markedly reduce the fatigue life; this effect was attributed to impact-induced residual stresses, microstructural distortion, geometric stress concentrations, and, most importantly, incipient microcrack formation. Threshold conditions for HCF failures following FOD can be described in terms of a modified Kitagawa–Takahashi approach, in terms of the smooth-bar fatigue limit, corrected for the stress concentration of the FOD indent and residual stresses, at small crack sizes and the worst-case threshold-stress intensity at larger continuum-sized crack sizes. Resistance to FOD-induced HCF failures was comparable in the bimodal and lamellar microstructures, although the lamellar microstructure was more prone to the formation of microcracks following high-velocity impact damage.

ACKNOWLEDGMENTS

This work was supported by the United States Air Force Office of Scientific Research under Grant No. F49620-96-1-0478 under the auspices of the Multidisciplinary University Research Initiative on *High Cycle Fatigue* to the University of California at Berkeley. One of the authors (BLB) acknowledges the support of the Hertz Foundation. Special thanks are due to Professor Werner Goldsmith for providing the compressed-gas gun facility, to Professor J.W. Hutchinson and Drs. J.M. McNaney, O. Roder, I. Altenberger, X. Chen, and A.W. Thompson for helpful discussions, and to Z. Bell, J.L. Hendricks, and C.K. Lau for their experimental assistance.

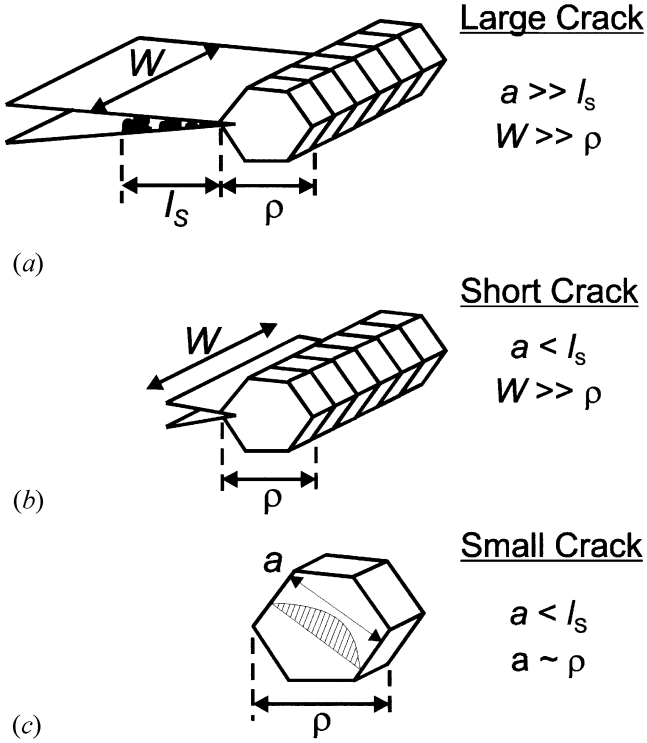

Fig. A1—Schematic illustrations highlighting the key distinctions between large, short, and small fatigue cracks. (*a*) Large cracks have length, *a*, and width, *W*, which are large both with respect to the equilibrium shielding-zone length, l_s (indicated here as a region of debris in the crack wake which produces crack closure), and the characteristic microstructural size scale, ρ, *e.g.*, the grain size. In contrast to this, (*b*) short fatigue cracks are characterized by $a < l_s$, but $W \gg \rho$. The reduced crack-wake length results in a lower level of crack-tip shielding. (*c*) for small cracks, the fracture surface is reduced in both dimensions, with *a* (and *W*) being small with respect to both l_s and ρ. The fact that $a \sim \rho$ implies that the crack front samples only a few microstructural entities, leading to a biased sampling of the microstructure. It should be noted here that owing to the coarser microstructure in the lamellar case, a crack belonging to class (c) for this microstructural condition can be over an order of magnitude larger than similar cracks in the bimodal case.

APPENDIX
Distinction between large, short, and small cracks

A key component of the present work is a comparison of the crack-growth behavior for fatigue cracks of varying dimension, which are classified here as *large*, *short*, and *small* cracks. For the sake of clarity, the salient differences between such cracks are briefly reviewed here. Large fatigue cracks (Figure A1(a)) have fracture surface dimensions that are large compared to the scale of the microstructure in both directions. Therefore, they generally have a fully developed* crack-tip shielding zone and can "sample" the microstructure in a statistical (continuum) manner.[63] With respect to large cracks, small cracks are generally described as being comparable in size to the following:[74]

*For mixed-mode loading conditions, the shearing of the fracture surfaces with respect to one another can produce crack-wake contact *via* sliding interference over dimensions that are much larger than for mode 1 loading, perhaps over the entire wake of a large fatigue crack.[68,70] Thus, the notion of a "fully developed" shielding zone is somewhat unclear for mixed-mode loading conditions. At the least, one would expect the equilibrium shielding-zone length to be a function of the applied ratio of shear to tension.

- microstructural dimensions, where biased statistical sampling of the microstructure can lead to accelerated crack advance along "weak" paths, *i.e.*, microstructural features oriented for easy crack growth (a continuum limitation);
- the extent of local inelasticity *ahead* of the crack tip, where the assumption of small-scale yielding implicit in the use of the stress intensity, K, is not strictly valid (a linear-elastic fracture mechanics limitation); and
- the extent of crack-tip shielding (*e.g.*, crack closure) *behind* the crack tip, where the reduced role of shielding leads to a higher local driving force than the corresponding large crack at the same applied K level (a similitude limitation).

However, a further important distinction can be made, namely, that of a short vs. small crack, as shown schematically in Figure A1. This distinction alludes not simply to physical size but the extent to which a fatigue crack is subjected to the first and third factors listed previously. Short fatigue cracks (Figure A1(b)) are physically short in only one dimension, a condition that is often realized experimentally by machining away the wake of a large crack. This type of fatigue flaw experiences limited crack-tip shielding due to its reduced length[35] yet still samples the microstructure as a continuum because of its extensive crack front. In contrast, small fatigue cracks (Figure A1(c)) are small and comparable to the microstructural size scale in all dimensions, as typified by the small, semielliptical surface flaw (*e.g.*, Reference 74). With such cracks, crack-tip shielding is significantly reduced (*e.g.*, Reference 63), and, since the crack front samples only few microstructural entities, this allows for a biased sampling of microstructurally weak paths. Because of this restriction in shielding and the biased microstructural sampling, fatigue-crack growth resistance in the presence of small cracks tends to be lowest.

REFERENCES

1. *Report of the AdHoc Committee on Air Force Aircraft Jet Engine Manufacturing and Production Processes*, United States Air Force Scientific Advisory Board, SAF/AQQS: the Pentagon, Washington, DC, 1992.
2. B.A. Cowles: *Int. J. Fracture*, 1996, vol. 80, pp. 147-63.
3. J.C.I. Chang: Air Force Office of Scientific Research, Bolling AFB, Washington, DC, 1996.
4. T. Nicholas, J.R. Barber, and R.S. Bertke: *Exp. Mech.*, 1980, vol. 20, pp. 357-64.
5. *Fretting Fatigue*, European Structural Integrity Society Publication No. 18, R.B. Waterhouse and T.C. Lindley, eds., Mechanical Engineering Publications Ltd., London, 1994.
6. J.J. Kruzic, J.P. Campbell, and R.O. Ritchie: *Acta Mater.*, 1999, vol. 47, pp. 801-16.
7. G. Lütjering: *Mater. Sci. Eng.*, 1998, vol. A243, pp. 32-45.
8. A.W. Thompson: in *Fatigue Behavior of Titanium Alloys*, R.R. Boyer, D. Eylon, and G. Lütjering, eds., TMS, Warrendale, PA, 1999, pp. 23-30.
9. J.C. Williams and G. Lütjering: in *Titanium '80, Science and Technology*, H. Kimura and O. Izumi, eds., TMS-AIME, Warrendale, PA, 1981, vol. 1, pp. 671-81.
10. J.J. Lucas: in *Titanium Science and Technology*, R.I. Jaffee and H.M. Burte, eds., Plenum Press, New York, NY, 1973, vol. 3, pp. 2081-95.
11. M. Peters, A. Gysler, and G. Lütjering: *Metall. Trans. A*, 1984, vol. 15A, pp. 1597-1605.
12. G. Lütjering, J. Albrecht, and A. Gysler: in *Titanium '92: Science and Technology*, F.H. Froes and I. Caplan, eds., TMS, Warrendale, PA, 1993, pp. 1635-46.
13. C.W. Brown and M.A. Hicks: *Fatigue Eng. Mater. Struct.*, 1983, vol. 6, pp. 67-76.
14. J.A. Hines, J.O. Peters, and G. Lütjering: in *Fatigue Behavior of Titanium Alloys*, R.R. Boyer, D. Eylon, and G. Lütjering, eds., TMS, Warrendale, PA, 1999, pp. 15-22.
15. J.C. Chesnutt, A.W. Thompson, and J.C. Williams: in *Titanium '80, Science and Technology*, H. Kimura and O. Izumi, eds., TMS-AIME, Warrendale, PA, 1981, vol. 2, pp. 1875-82.
16. G.R. Yoder, L.A. Cooley, and T.W. Crooker: *Eng. Fract. Mech.*, 1983, vol. 17, pp. 185-88.
17. G.R. Yoder, L.A. Cooley, and T.W. Crooker: *Metall. Trans. A*, 1977, vol. 8A, pp. 1737-43.
18. K.S. Ravichandran: *Acta Mater.*, 1991, vol. 39, pp. 401-10.
19. P.E. Irving and C.J. Beevers: *Mater. Sci. Eng.*, 1974, vol. 14, pp. 229-38.
20. G.R. Yoder, L.A. Cooley, and T.W. Crooker: *Eng. Fract. Mech.*, 1979, vol. 11, pp. 805-16.
21. D. Taylor: *A Compendium of Fatigue Thresholds and Crack Growth Rates*, EMAS Ltd., Warley, United Kingdom, 1985.
22. J.K. Gregory: in *Handbook of Fatigue Crack Propagation in Metallic Structures*, A. Carpinteri, ed., Elsevier Science B.V., Amsterdam, The Netherlands, 1994, pp. 281-21.
23. M.R. Bache, W.J. Evans, and M. McElhone: *Mater. Sci. Eng.*, 1997, vols. A234-A236, pp. 918-22.
24. J.P. Thomas: *Scripta Mater.*, 1998, vol. 39, pp. 1647-52.
25. J.W. Sheldon, K.R. Bain, and J.K. Donald: *Int. J. Fatigue*, 1999, vol. 21, pp. 733-41.
26. Y.N. Lenets and R.S. Bellows: *Int. J. Fatigue*, 2000, vol. 22, pp. 521-29.
27. R.O. Ritchie: in *Proc. ASME Aerospace Division*, J.C.I. Chang, J. Coulter, D. Brei, D. Martinez, W. Hg, and P.P. Freidmann, eds., ASME, New York, NY, 1996, AMD vol. 52, pp. 321-33.
28. D. Eylon: *Summary of Available Information on the Processing of the Ti-6Al-4V HCF/LCF Program Plates*, University of Dayton Report, Dayton, OH, 1998.
29. J.C. Chesnutt, A.W. Thompson, and J.C. Williams: *Technical Report No. AFML-TR-78-68*, Air Force Materials Laboratory, Wright-Patterson Air Force Base, OH, 1978.
30. R.O. Ritchie, D.L. Davidson, B.L. Boyce, J.P. Campbell, and O. Roder: *Fat. Fract. Eng. Mater. Struct.*, 1999, vol. 22, pp. 621-31.
31. B.L. Boyce and R.O. Ritchie: *Eng. Fract. Mech.*, 2001, vol. 68, pp. 129-47.
32. H. Döker, V. Bachmann, and G. Marci: in *Fatigue Thresholds*, J. Bäcklund, A.F. Blom and C.J. Beevers, eds., EMAS, Warley, United Kingdom, 1982, vol. 1, pp. 45-58.
33. W.A. Herman, R.W. Hertzberg, and R. Jaccard: *Fatigue Fract. Eng. Mater. Struct.*, 1988, vol. 11, pp. 303-20.
34. H.R. Mayer and S.E. Stanzl-Tschegg: BOKU, Vienna, Austria, unpublished research, 1998.
35. R.O. Ritchie and W. Yu: in *Small Fatigue Cracks*, R.O. Ritchie and J. Lankford, eds., TMS-AIME, Warrendale, PA, 1986, pp. 167-89.
36. P. Lukáš: *Eng. Fract. Mech.*, 1987, vol. 26, pp. 471-73.
37. J.C. Newmann and I.S. Raju: *Eng. Fract. Mech.*, 1981, vol. 15, pp. 185-92.
38. K.S. Ravichandran: *Metall. Mater. Trans. A*, 1997, vol. 28A, pp. 149-56.
39. K.S. Ravichandran and J.M. Larsen: *Metall. Mater. Trans. A*, 1997, vol. 28A, pp. 157-69.
40. J.O. Peters, O. Roder, B.L. Boyce, A.W. Thompson, and R.O. Ritchie: *Metall. Mater. Trans. A*, 2000, vol. 31A, pp. 1571-83.
41. B.L. Boyce: Ph.D. Thesis, R.O. Ritchie, advisor, University of California, Berkeley, CA, Dec. 2001.
42. M.Y. He and J.W. Hutchinson: *J. Appl. Mech.*, 2000, vol. 67, pp. 207-09.
43. J.P. Campbell and R.O. Ritchie: *Eng. Fract. Mech.*, 2000, vol. 67, pp. 209-27.
44. J.P. Campbell and R.O. Ritchie: *Eng. Fract. Mech.*, 2000, vol. 67, pp. 229-49.
45. J.P. Campbell and R.O. Ritchie: *Metall. Mater. Trans. A*, 2001, vol. 32A, pp. 497-503.
46. M.Y. He and J.W. Hutchinson: *Eng. Fract. Mech.*, 2000, vol. 65, pp. 1-14.
47. J.O. Peters and R.O. Ritchie: *Eng. Fract. Mech.*, 2000, vol. 67, pp. 193-207.
48. J.O. Peters and R.O. Ritchie: *Int. J. Fatigue*, 2001, in press.
49. B.L. Boyce, X. Chen, J.W. Hutchinson, and R.O. Ritchie: *Mech. Mater.*, 2001, vol. 33, pp. 441-54.
50. D.L. Davidson and D. Eylon: *Metall. Trans. A*, 1980, vol. 11A, pp. 837-43.

51. M.R. Bache, W.J. Evans, and H.M. Davies: *J. Mater. Sci.*, 1997, vol. 32, pp. 3435-42.
52. Y. Murakami, T. Nomoto, and T. Ueda: *Fatigue Fract. Eng. Mater. Struct.*, 1999, vol. 22, pp. 581-90.
53. L. Wagner and G. Lütjering: *Proc. 2nd Int. Conf. Shot Peening*, H.O. Fuchs, ed., American Shot Peening Society, Paramus, NJ, 1984, pp. 194-200.
54. S. Adachi, L. Wagner, and G. Lütjering: *Titanium Science and Technology. Proc. 5th Int. Conf. on Titanium*, G. Lütjering, V. Zwicker, and W. Bunk, eds., DGM, Oberursel, Germany, 1985, p. 2139.
55. W.J. Evans and M.R. Bache: *Int. J. Fatigue*, 1994, vol. 16, pp. 443-52.
56. G. Marci: in *Fatigue '96, Proc. 6th Int. Congr. on Fatigue*, G. Lütjering and H. Nowack, eds., Pergamon Press, Oxford, United Kingdom, 1996, vol. I, p. 493.
57. R.J.H. Wanhill: *Corrosion-NACE*, 1974, vol. 30, pp. 28-35.
58. D.B. Dawson and R.M.N. Pelloux, *Metall. Trans*, 1974, vol. 5, pp. 723-31.
59. M.D. Halliday and C.J. Beevers: *J. Testing Eval.*, 1981, vol. 9, pp. 195-201.
60. K.S. Ravichandran: *Scripta Metall. Mater.*, 1990, vol. 24, pp. 1559-63.
61. T. Ogawa, K. Tokaji, and K. Ohya: *Fatigue Fract. Eng. Mater. Struct.*, 1993, vol. 16, pp. 973-82.
62. V. Sinha, C. Mercer, and W.O. Soboyejo: *Mater. Sci. Eng.*, 2000, vol. A287, pp. 30-42.
63. S. Suresh and R.O. Ritchie: *Int. Met. Rev.*, 1984, vol. 29, pp. 445-76.
64. M.A. Pustejovsky: *Eng. Fract. Mech.*, 1979, vol. 11(1), pp. 9-15.
65. M.A. Pustejovsky: *Eng. Fract. Mech.*, 1979, vol. 11(1), pp. 17-31.
66. H. Gao, M.W. Brown, and K.J. Miller: *Fat. Eng. Mater. Struct.*, 1982, vol. 5, pp. 1-17.
67. J. Tong, J.R. Yates, and M.W. Brown: *Fat. Eng. Mater. Struct.*, 1994, vol. 17, pp. 829-38.
68. H. Nayeb-Hashemi, F.A. McClintock, and R.O. Ritchie: *Metall. Trans. A*, 1982, vol. 13A, pp. 2197-204.
69. M.C. Smith and R.A. Smith: in *Basic Question in Fatigue: vol. 1, ASTM STP 924*, J.T. Fong and R.J. Fields, eds., ASTM, Philadelphia, PA, 1988, pp. 260-80.
70. E.K. Tschegg: *Acta Metall.*, 1983, vol. 31, pp. 1323-30.
71. J.O. Peters, B.L. Boyce, X. Chen, J.M. McNaney, J.W. Hutchinson, and R.O. Ritchie: *Proc. Int. Conf. Fatigue in the Very High Cycle Regime*, S. Stanzl-Tschegg and H. Mayer, eds., BOKU, Vienna, Austria, 2001, pp. 129-40.
72. H. Kitagawa and S. Takahashi: *Proc. 2nd Intl. Conf. on Mechanical Behavior of Materials*, ASM, Metals Park, OH, 1976, pp. 627-31.
73. M.H. El Haddad, T.H. Topper, and K.N. Smith: *Eng. Fract. Mech.*, 1979, vol. 11, pp. 573-84.
74. R.O. Ritchie and J. Lankford: *Mater. Sci. Eng.*, 1986, vol. 84, pp. 11-16.